Monthly Notices
of the
ROYAL ASTRONOMICAL SOCIETY

MNRAS **460,** 1954–1969 (2016)
Advance Access publication 2016 May 10

doi:10.1093/mnras/stw1033

The nature of the torus in the heavily obscured AGN Markarian 3: an X-ray study

M. Guainazzi,[1,2★] G. Risaliti,[3,4] H. Awaki,[5] P. Arevalo,[6] F. E. Bauer,[7,8,9] S. Bianchi,[10] S. E. Boggs,[11] W. N. Brandt,[12,13,14] M. Brightman,[15] F. E. Christensen,[16] W. W. Craig,[11,17] K. Forster,[15] C. J. Hailey,[18] F. Harrison,[15] M. Koss,[19] A. Longinotti,[20] C. Markwardt,[21] A. Marinucci,[10] G. Matt,[10] C. S. Reynolds,[22] C. Ricci,[7] D. Stern,[23] J. Svoboda,[24] D. Walton[15,23] and W. Zhang[21]

Affiliations are listed at the end of the paper

Accepted 2016 April 28. Received 2016 April 28; in original form 2016 March 7

ABSTRACT

In this paper, we report the results of an X-ray monitoring campaign on the heavily obscured Seyfert galaxy, Markarian 3, carried out between the fall of 2014 and the spring of 2015 with *NuSTAR*, *Suzaku* and *XMM–Newton*. The hard X-ray spectrum of Markarian 3 is variable on all the time-scales probed by our campaign, down to a few days. The observed continuum variability is due to an intrinsically variable primary continuum seen in transmission through a large, but still Compton-thin column density ($N_{\rm H} \sim 0.8$–1.1×10^{24} cm^{-2}). If arranged in a spherical-toroidal geometry, the Compton scattering matter has an opening angle $\simeq 66^{\circ}$, and is seen at a grazing angle through its upper rim (inclination angle $\simeq 70^{\circ}$). We report a possible occultation event during the 2014 campaign. If the torus is constituted by a system of clouds sharing the same column density, this event allows us to constrain their number (17 ± 5) and individual column density, [$\simeq (4.9 \pm 1.5) \times 10^{22}$ cm^{-2}]. The comparison of IR and X-ray spectroscopic results with state-of-the art 'torus' models suggests that at least two-thirds of the X-ray obscuring gas volume might be located within the dust sublimation radius. We report also the discovery of an ionized absorber, characterized by variable resonant absorption lines due to He- and H-like iron. This discovery lends support to the idea that moderate column density absorbers could be due to clouds evaporated at the outer surface of the torus, possibly accelerated by the radiation pressure due to the central AGN emission leaking through the patchy absorber.

Key words: galaxies: active – galaxies: Seyfert – X-rays: galaxies – X-rays: individual: Markarian 3.

1 INTRODUCTION

A breakthrough in our understanding of the physical properties and geometrical configuration of gas and dust in the innermost parsec around accreting supermassive black holes came recently from dust reverberation experiments in the near-infrared (NIR). By measuring the response of hot dust emission to changes in the ionizing continuum, it has been possible to determine the typical size of the innermost boundary of the dusty 'torus' in about 20 nearby active galactic nuclei (AGN; Suganuma et al. 2006; Kishimoto et al. 2007; Koshida et al. 2014; Pozo-Nuñez et al. 2014; Jun et al. 2015). Coupled with imaging NIR and mid-IR interferometry (Jaffe et al. 2004; Burtscher et al. 2013) and models of 'clumpy tori' (Nenkova et al. 2008), these observational results set unprecedented constraints on the structure and location of the azimuthally symmetric obscuring material invoked by 'unification-by-orientation' AGN scenarios (Antonucci & Miller 1985; Antonucci 1993; Netzer 2015). The most important collective result of these experiments is the discovery of a scaling law between the spatial scale of the innermost region of the host dust and the continuum luminosity. Whenever measurements in the NIR are available together with optical reverberation mapping results, the hot dust spatial scale is larger by a factor of about 3 than the optical broad-line region (BLR). This vindicates the old idea that the outermost region of the BLR is set by the dust sublimation radius (Netzer & Laor 1993).

However, IR measurements probe only the dusty phase of the obscuring matter in the AGN environment. In order to obtain the full

★ E-mail: Matteo.Guainazzi@sciops.esa.int

picture, X-ray measurements are required. X-rays probe emission (and therefore its obscuration) along the line of sight to the central engine down to scales on the order of a few gravitational radii from the event horizon (Risaliti et al. 2005; Chartas et al. 2009; Morgan et al. 2012). Serendipitous X-ray occultation measurements demonstrate that highly dynamical systems of X-ray obscuring clouds are present at all scales from the innermost region of the BLRs to the torus (Bianchi, Maiolino & Risaliti 2012; Markowitz, Krumpe & Nikutta 2014; Torricelli-Ciamponi et al. 2014).

In 2012, Guainazzi et al. (2012; G12) analysed all the *XMM–Newton*, *Suzaku* and *Swift* X-ray observations of the nearby ($z = 0.014$) AGN Markarian 3 performed in this century. Known since the dawn of X-ray astronomy, Markarian 3 hosts a heavily obscured AGN (Cappi et al. 1999) with a Seyfert 2 optical classification (Khachikian & Weedman 1974). The most prominent feature in its X-ray spectrum is a strong iron Kα fluorescent line (Awaki et al. 1991). The relation between the Fe Kα equivalent width (EW; $\simeq$1000 eV) and the ratio between the X-ray and the Balmer-corrected [O III] flux ($\sim$0.14) is consistent with a heavily obscured Compton-thin, or with a Compton-thick AGN (Bassani et al. 1999).[1] While the soft X-ray emission stayed constant (within the flux cross-calibration uncertainties among different observatories) over the last 15 yr (as well as during a prior 13 yr campaign discussed by Iwasawa et al. 1994), the hard X-ray flux above 4 keV showed significant variability down to time-scales as short as two months. Moreover, assuming that the light curves in the 3–5 keV and 15–150 keV energy bands are correlated, the former lagged the latter with a minimum measured delay of $\gtrsim$1200 d (G12). These experimental results together with the discovery of extended hard ($E \gtrsim 3$ keV) X-ray emission on scales of $\simeq$300 pc suggested that the X-ray emission in Markarian 3 could directly probe the clumpy nature of the gas and dusty phase of the obscuring matter in AGN.

However, the results published in G12 were primarily based on spectra taken at energies lower than 10 keV. This affected their results in two ways: (1) it did not allow them to probe the line-of-sight column density simultaneously with the spectral component associated with Compton scattering of the global distribution of clouds surrounding the AGN; (2) it did not fully remove uncertainties regarding the uniqueness of the spectral decomposition, due to the expected spectral complexity in the energy range where the analysis was possible. Moreover, the observations of Markarian 3 taken before 2012 covered a sparse time pattern, inadequate to determine variability time-scales.

Recently, Yaqoob et al. (2015) challenged G12's interpretation of the X-ray light curve of Markarian 3 on different astrophysical grounds. They showed that the G12 interpretation was primarily driven by using models for the reflection continuum with an infinite matter column density. Using models that fit explicitly the global column density of the reflector and treat self-consistently the reprocessing of the X-ray continuum and the X-ray fluorescence, Yaqoob et al. (2015) found a line-of-sight column density significantly lower than the Compton-thick limit. This result falsifies the basic assumption in G12, i.e. that the 4–5 keV energy band can be used to probe the reprocessing matter.

In order to overcome the sparse sampling of the existing archival data, an observational campaign on Markarian 3 was designed and carried out between autumn 2014 and spring 2015, based on *NuSTAR* (Harrison et al. 2013). Thanks to its hard X-ray focusing optics, *NuSTAR* allows a giant leap in sensitivity above 10 keV when compared to any prior X-ray observatories. In this paper, we present the main results of this campaign, characterizing the properties of the obscuring gas and dust surrounding the nuclear environment of this archetypical obscured AGN. Besides regular monitoring of Markarian 3 with *NuSTAR*, the campaign included quasi-simultaneous observations with the CCD detectors on board *Suzaku* and *XMM–Newton*, providing better energy resolution at the energy of the iron atomic transitions. We also present in this paper a reanalysis of the 2005 *Suzaku* data originally discussed by Awaki et al. (2008), as well as archival *Chandra*/High-Energy Transmission Grating (HETG) data at the highest available spectral resolution in the iron energy band.

The paper is organized as follows: we describe the observational campaign in Section 2. The data reduction and spectral analysis are described in Section 3. The results of the spectral analysis are presented in Section 4. We discuss our findings in Section 5, and summarize them in Section 6. The following cosmological parameters were used to calculate luminosities: $H_0 = 70$ km s^{-1} Mpc^{-1}, $\Lambda_0 = 0.73$, and $\Omega_{\rm M} = 0.27$ (Bennett et al. 2003) to ease comparison with G12. With this choice, 1 arcsec corresponds to 270 pc at the distance of Markarian 3.

2 THE OBSERVATIONAL CAMPAIGN

The *NuSTAR* monitoring campaign on Markarian 3 was divided into two seasons. A first series of five observations was performed between 2014 September 7 and October 23. The time separation between consecutive observations ranges between 7 and 22 d. Prompted by the discovery of variability between observations separated by the shortest time interval, a second observational campaign was organized for Winter–Spring 2015. Four additional observations were performed between 2015 March 19 and April 8, with a minimum separation of three days between consecutive observations. Table 1 presents a log of the observations discussed in this paper.

Whenever possible, *Suzaku* or *XMM–Newton* observations were planned quasi-simultaneously with *NuSTAR*. This was possible on 2014 October 1, October 23 with *Suzaku* and 2015 March 23, and on 2015 March 19 and April 8 with *XMM–Newton*. The *XMM–Newton* observations were performed at the end of the 48-h spacecraft orbit, close to the radiation belts. The exposure times were therefore shorter than 1 h, compared to the 4–7 h of the *NuSTAR* and *Suzaku* observations. Despite the low signal to noise, the inclusion of the EPIC-pn spectrum in the fit improves the precision in the determination of the Fe Kα centroid energy by $\simeq$25 per cent in the April 8 observation (from $\Delta E \simeq 40$ eV to $\Delta E \simeq 30$ eV), thanks to the better energy resolution of the CCD cameras. An additional *Suzaku* observation was performed on 2014 October 7. As this observation does not overlap with the closest *NuSTAR* observation (October 9), these data will not be discussed in this paper.

In this paper, spectra extracted from overlapping observations are analysed together. To maximize signal to noise, we did not attempt to find common good time intervals between overlapping observations. Spectral fits are typically dominated by *NuSTAR* due to the significantly larger number of collected photons. The CCD measurements provide primarily an independent check on the accuracy of the energy scale at the Fe emission line energies. Given the typical time-scales and spectral dynamical range, not using strictly simultaneous observations could, in principle, induce systematic

[1] Following the usual convention, we assume $N_{\rm H,\,th} \equiv \sigma_{\rm t}^{-1} \simeq 1.5 \times 10^{24}$ cm^{-2} as the column density threshold separating Compton-thin from Compton-thick AGN, where $\sigma_{\rm t}$ is the Thompson scattering cross-section.

Table 1. Log of the observations discussed in this paper. In the fifth column: 'S' = *Suzaku*; 'X' = *XMM–Newton*.

Obs.#	Start time	T_{exp} (ks)	Obs.#	Start time	T_{exp} (ks)
NuSTAR			Quasi-simultaneous with...		
60002048002	2014-09-07T17:26:07	30.0	–	–	–
60002048004	2014-09-14T10:51:07	33.5	–	–	–
60002048006	2014-10-01T12:41:07	33.2	709022010 (S)	2014-10-01T22:08:01	20.6
60002048008	2014-10-09T04:36:07	26.5	–	–	–
60002048010	2014-10-23T06:01:07	30.9	709022030 (S)	2014-10-23T03:37:31	20.3
60002049002	2015-03-19T12:46:07	23.2	0741050101(X)	2015-03-19T17:55:25	3.1
60002048012	2015-03-23T05:31:07	26.7	709022040 (S)	2015-03-23T05:48:56	18.7
60002049004	2015-04-05T01:31:07	24.7	–	–	–
60002049006	2015-04-08T08:36:07	25.2	0741050201 (X)	2015-04-08T16:46:38	3.8

uncertainties in the derived spectral parameters. However, we estimate that this uncertainty is smaller than the statistical errors.

3 DATA REDUCTION

3.1 *NuSTAR*

NuSTAR data were reduced using the software suite available in HEASOFT version 6.16, using the CALibration DataBase version 1.1 (2015 March 16). Calibrated event lists were produced with `nupipeline` version 0.43. Light curves and spectra were generated with `nuproducts` 0.2.8, using standard data selection criteria. Observations with *Chandra* ACIS unveiled extended emission ±2 arcsec in size along a E-W axis aligned with the E-W optical narrow-line regions (NLR) in the soft X-ray band (Sako et al. 2000) with fainter emission extending up to 15 arcsec in radius. The iron line emission could also be similarly extended (G12). This means that the X-ray emission of Markarian 3 is basically point-like for the *NuSTAR* telescopes' point spread function (PSF, 60 arcsec half-power diameter; Madsen et al. 2015). We therefore extracted source plus background photons from a 122 arcsec radius circular regions centred on the nominal optical coordinates of the AGN (α_{2000} = 6:15:36.316, δ_{2000} = +71:02:12.51; J2000). Besides the emission from the Markarian 3 AGN, the *Chandra* ACIS image shows three additional point sources in the *NuSTAR* aperture. These sources are not detected above the background fluctuations in a $E > 4$ keV ACIS-S image of the Markarian 3 field taken in 2013, January 13 (when the image of Markarian 3 comprised about 2000 counts). Their distances from the Markarian 3 nucleus are between 50 and 110 arcsec. They would be detected at least as a distortion of the *NuSTAR* PSF, or as a displacement of its centroid if they would significantly contribute to the observed flux during the *NuSTAR* observations. We estimate that their contribution to the flux above 4 keV in the *NuSTAR* aperture is $\ll$1 per cent during the monitoring campaign discussed in this paper. Background spectra were extracted from 84 arcsec circular regions around the sky coordinates (α_{2000} = 6:16:31.307, δ_{2000} = +71:02:54.05), after checking that this region is free from serendipitous contaminating sources in the 3–80 keV *NuSTAR* images. The total counts in the background regions in the different observations are consistent with pure Poissonian distributions whose mean, μ, and variance, σ^2, agree within 0.3 per cent. No spatial gradient is seen in the background images. The fraction of the background counts with respect to the source plus background counts is $\simeq$1 per cent at 6 keV, and $\simeq$10 per cent at 50 keV (Fig. 1).

The *NuSTAR* 3–50 keV light curve shows large-amplitude variability with a dynamical range larger than a factor of 2 (Fig. 2).

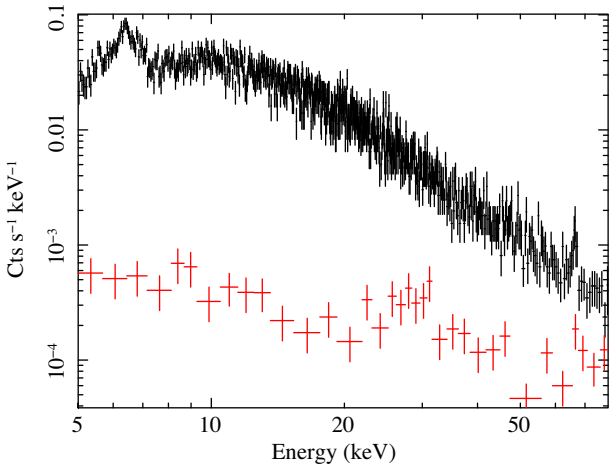

Figure 1. Comparison between the source plus background (top; black) and the background *NuSTAR* spectrum (bottom; red) for Obs.#60002049002, corresponding to the lowest *NuSTAR* count rate measured during the Markarian 3 2014–2015 campaign.

The largest flux changes ($\simeq$70 per cent) occurred between the second (2014 September 14) and the third (2014 October 1) epochs. We extracted the light curves from each individual observation in the 3–7 keV, 7–15 keV, and 15–50 keV energy bands to check for any significant inter-observation flux variability. As a crude variability estimate, we calculated the reduced χ^2 when fitting each light curve with a constant. In only four light curves is χ^2 larger than the $1/N_{lc}$ percentage point, where $N_{lc} = 27$ is the total number of light curves (3 energy ranges times 9 observations): the 7–15 keV light curve on 2015 March 19, and the 15–50 keV light curves on 2014 September 7, 2015 March 19, and 2015 April 5. In all cases, the comparatively high values of χ^2 are dominated by individual bins with a low effective exposure. We therefore conclude that inter-observation variability does not affect the results discussed in this paper.

3.2 *Suzaku*

We followed the *Suzaku* data reduction procedure as described in G12. Briefly, we used the *Suzaku* data analysis software included in HEASOFT version 6.16, and CALDB version 1.1 (2014 October 10). Data were reduced, and spectral products and responses were extracted following the same procedures as in Awaki et al. (2008). Due to spacecraft battery re-charging issues, the hard X-ray detector (HXD) was switched off during all the observations of the Markarian 3 monitoring campaign. Only data obtained with the

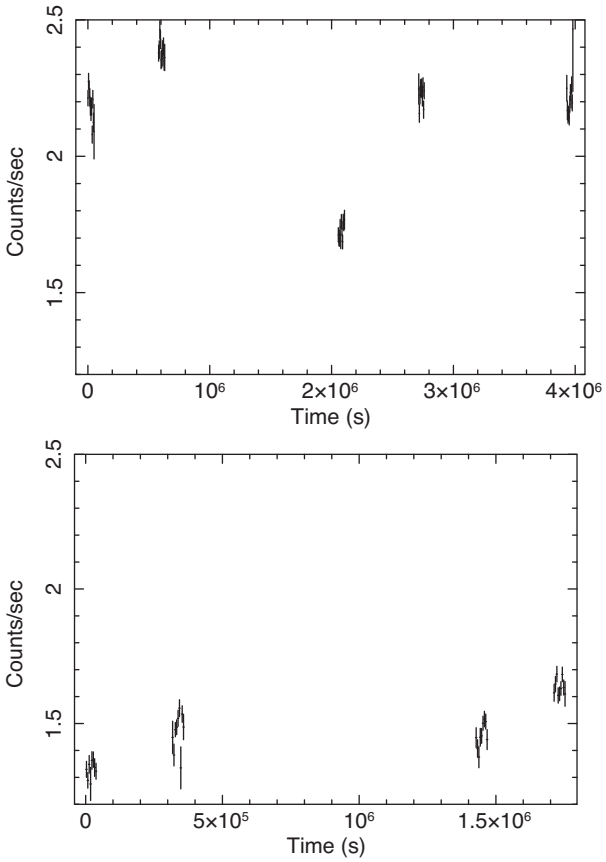

Figure 2. 3–50 keV *NuSTAR* light curve of Markarian 3 during the 2014 (upper) and 2015 (lower) observational campaigns. The binning time is 5000 s. The light curves are shown on the same *y*-axis scale to ease comparison. Error bars represent 1σ level uncertainties.

CCD cameras on-board *Suzaku* (X-ray Imaging Spectrometer, XIS; Koyama et al. 2007) are therefore discussed in this paper. Source plus background spectra were extracted from circular regions centred on the X-ray source centroid, using a radius between about 190 and 240 arcsec to optimize the signal to noise of each individual observation. Background spectra were extracted from circular regions on the same camera chip, avoiding the region in detector coordinates illuminated by the calibration source, as well as serendipitous contaminating sources in the XIS field of view – in particular, IXO-30 (Bianchi et al. 2005b; Pounds & Page 2005). We merged together the spectra of the operational front-illuminated CCDs (XIS0 and XIS3; 'FI' chips hereafter), but fit separately the spectra of the front- and back-illuminated units due to their different responses.

3.3 *XMM–Newton*

Also for the *XMM–Newton* data, we followed the same data reduction procedure as in G12. Because we are interested in the variability properties of Markarian 3 in the hard X-ray band (i.e., above 4 keV), we do not discuss the high-resolution Reflection Grating Spectrometer data in this paper. Furthermore, we consider only spectra extracted with the CCD EPIC-pn camera (Strüder et al. 2001), due to its higher effective area. Calibrated event lists, spectra and responses were generated with SAS version 14 (Gabriel et al. 2003), using the most updated calibration files available at the time the data reduction was performed (2015 April). Source plus background spectra were extracted from circular regions of 30 arcsec radius. Background spectra were generated from circular regions of 60 arcsec radius, extracted from the same CCD and at the same height in detector coordinates as the source to ensure that the same charge transfer inefficiency correction applies, because this correction depends on the distance from the readout node.

3.4 Spectra handling

In fitting the spectra, we employed the Cash goodness-of-fit statistic (Cash 1976), that is the appropriate maximum likelihood for Poissonian data. More specifically, we employed the W-statistics implemented in XSPEC v12.8.2 (Arnaud 1996) through the command `statistic cstat` when source plus background and background spectra are used. In order for the algorithm to work properly, we rebinned the source plus background spectra to ensure that each spectral channel has at least one count (Arnaud, private communication). We did not attempt at modelling the background spectra, due to their complexity and not fully understood time-variability. We used instead the approach, standard in X-ray astronomy, of subtracting from the source plus background spectrum an appropriately rescaled background spectrum prior to applying the forward-folding spectral fitting algorithm. Unless otherwise specified, statistical uncertainties are quoted hereafter at the 90 per cent confidence level for one interesting parameter (Lampton, Margon & Bowyer 1976). We fit the CCD spectra in the 4–10 keV energy range, while the *NuSTAR* spectra are fit in the 5–79 keV energy range, where the response is well calibrated (Madsen et al. 2015).

The spectra analysed in this paper were extracted from sky regions sharing the same centroid, but whose size was optimized to obtain the best signal to noise for each instrument. The difference in size could in principle introduce spurious variability when comparing observations taken with different instruments at different epochs. However, we are confident that this effect is negligible on the following grounds: (1) at all epochs at least a pair of *NuSTAR* spectra were analysed. These spectra were extracted from the same regions in sky coordinates. They dominate the statistics of the spectral fits. Fluxes and luminosities in this paper are calculated from the *NuSTAR* best-fitting models; (2) models fitting the *Suzaku*/XIS and *XMM–Newton*/EPIC spectra were multiplied by constant factors to take into account possible differences in the instrumental cross-calibration. These factors are always $\leq$10 per cent, consistent with known calibration uncertainties (Ishida et al. 2011; Madsen et al. 2015); (3) while the hard X-ray emission of Markarian 3 is extended, the extension is of a few arcseconds at most, and its integrated flux is only a few per cent of the total flux (G12). For instruments with a moderate spatial resolution as those discussed in this paper, the hard X-ray emission of Markarian 3 is basically point-like. The measured counts are therefore properly corrected for the encircled energy fraction through the effective area when deriving intrinsic fluxes and luminosities.

4 DATA ANALYSIS

Fig. 3 shows the *NuSTAR* and *Suzaku*/XIS (FI chips only) spectra taken during the 2014–2015 monitoring campaign. Due to the stability of the instrumental responses (Koyama et al. 2007; Madsen et al. 2015) these count spectra can be directly compared to gauge qualitatively the hard variability pattern above 3 keV, where the XIS

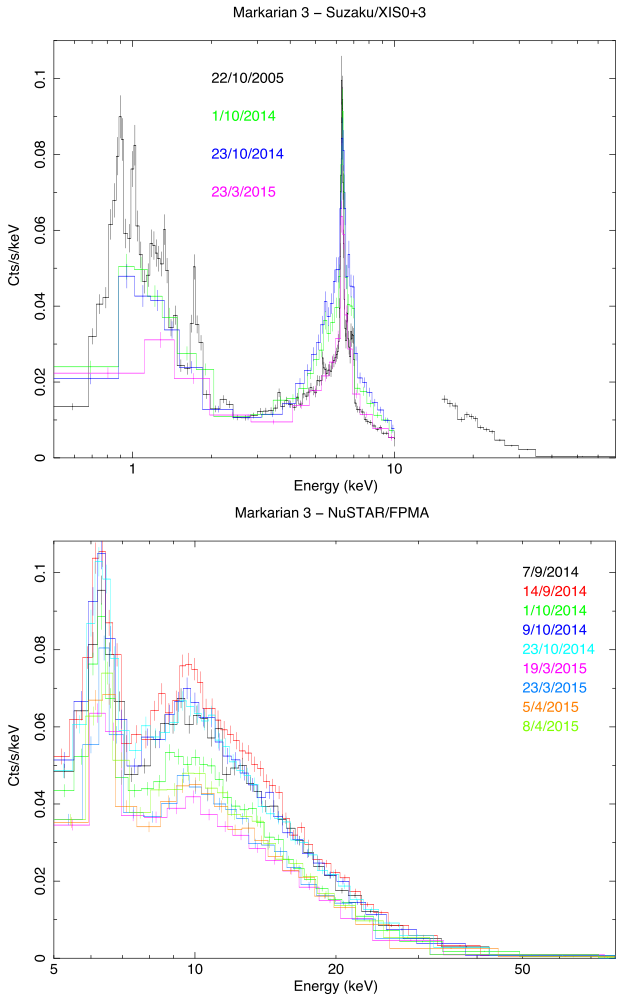

Figure 3. *Suzaku* FI-CCD (top) and *NuSTAR* (bottom) count spectra obtained during the 2014–2015 monitoring campaign. The labels indicate the observation start day. The *Suzaku* plot includes also the 2005 XIS and HXD observation. In this figure, the spectra are rebinned for clarity to a minimum signal-to-noise ratio of 10 per spectral channel (observation date color coding in the on-line version).

spectra show a dramatic count rate increase due to the emergence of the obscured AGN component.[2]

The *NuSTAR* spectra in Fig. 3 show a slight increase of the overall flux between September 7 and 14 was followed by a sharp $\simeq$70 per cent flux decrease in the following two weeks. The 2015 observations exhibit a lower flux than the 2014 ones. The lowest flux level was measured on March 19, followed by a slow gradual 20 per cent flux recovery until the last observation on April 8. Significant flux (7.7 $\pm$ 0.1 per cent) and spectral variability is observed down to the shortest time-scale probed by the monitoring campaign, i.e. the four days between April 19 and 23. It is the first time that hard X-ray variability on such a short time-scale is reported in Markarian 3. Prior studies estimated an upper limit of the hard X-ray variability time-scale of about two months (Iwasawa et al. 1994; G12).

[2] The *Suzaku*/XIS is known to be affected of a strongly time-variable molecular contamination layer. This layer, however, affects the response only below $\simeq$1 keV.

The comparison among the *Suzaku* FI-XIS count spectra allows us to better disentangle the variability pattern of the Fe Kα line and of the underlying continuum due to the better resolution of the CCD cameras at $\simeq$6 keV. The spectrum measured during the flux minimum on March 23 (*Suzaku* did not observe Markarian 3 on March 19) exactly overlaps with that measured during the deep *Suzaku* observation in 2005 (Awaki et al. 2008). This suggests that such a low-flux state corresponds to a high Compton-reflection versus primary flux fraction due to the expected stability of this spectral component on the time-scales probed by the 2014–2015 monitoring campaign (and confirmed a posteriori by the results discussed in this paper). The comparison between the *NuSTAR* March 19 and 23 spectra further suggests that the minimum flux state measured by *Suzaku* was preceded by a state with an even higher reflection fraction.

Even in the restricted energy decade discussed in this paper, the Markarian 3 spectrum is complex. In order to understand the contribution of each of these components to the observed variability pattern, and to elucidate the origin of the variability, the contribution of these components to the total spectrum must be quantitatively characterized. This is the goal of this section.

4.1 The soft X-ray spectrum

The soft (i.e. below $\simeq$2 keV) emission in Markarian 3 is dominated by an AGN-photoionized plasma (Bianchi et al. 2005b; Pounds et al. 2005), probably associated with the extended E-W structure observed by the *Chandra*/ACIS (Sako et al. 2000). This component contributes only a few per cent to the flux in the energy range used for spectral fitting in the following sections. However, even this small contribution may significantly bias the best-fitting results if not properly taken into account. We therefore decided to include components describing the soft X-ray emission in all the models described in this paper.

In order to achieve a model of the soft X-ray emission in Markarian 3, we fit the *Suzaku* XIS spectra of the deep 2005 observation in the 0.5–2 keV energy range (see Awaki et al. 2008 on the data reduction). A good spectral fit is obtained through the combination of one collisionally ionized optically thin plasma (`apec`; Foster et al. 2012), a power law, and two photoionized components, seen through a photoelectric absorption column density of 9.7 $\times$ 10^{20} cm^{-2}, equal to the estimated contribution of neutral gas in our Galaxy (Kalberla et al. 2005). We calculated the emission from a photoionized plasma using XSTAR (Kallman et al. 2014), after generating a level population file appropriate for the Markarian 3 X-ray spectral energy distribution (energy index, α, -0.8), and using a density $n_e = 10^4$ cm^{-3}, an average value of the spatially resolved model for the NLR gas in Markarian 3 (Collins et al. 2009). In this scenario, the power law may be due to electron scattering, not included in the XSTAR calculation of the reflection spectrum. The 2005 XIS soft X-ray spectrum and best-fitting model are shown in Fig. 4. The best-fitting parameters of the soft X-ray model are shown in Table 2. The fit is acceptable (C/ν = 1161.4/813). However, an emission-line feature around 1.7–1.8 keV remain unaccounted for. Formally, it can be fit with an unresolved Gaussian profile with centroid energy $E = 1.744 \pm 0.007$ keV and intensity $I = (6.5 \pm 1.0) \times 10^{-6}$ photons cm^{-2} s^{-1}. It could be due either to a $3p^1 \rightarrow 1s^1$ transition of Mg XI, or, more likely, to known calibration uncertainties at the energies of the XIS detector Silicon edge or escape peak. The addition of further photoionized or collisionally ionized components, even if we allow the elemental abundance to be a free parameter in the fit, yield a negligible further improvement in the

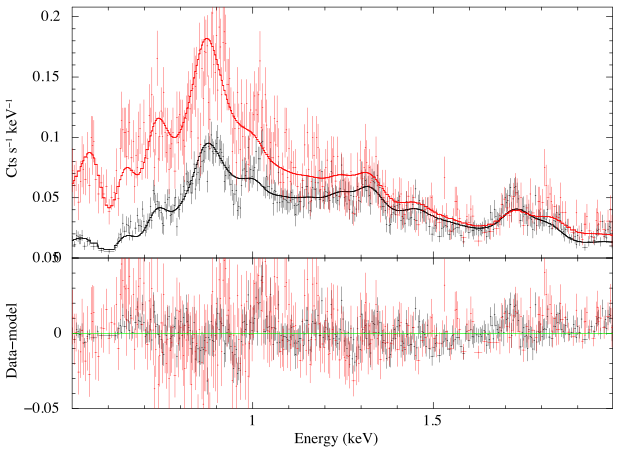

Figure 4. Upper panel; *Suzaku* BI (red, upper data) and FI-XIS (black, lower data) Markarian 3 2005 spectra (crosses) and best-fitting model (line) in the 0.5–2 keV energy band. Lower panel: residuals against the best fit. Spectral units in this and similar subsequent figures are counts per second per energy (keV).

Table 2. Best-fitting parameters of the soft X-ray model employed in this paper.

Photoionized components	
$\log(\xi_{1,\,\mathrm{cgs}})$	<-0.7
$N_{\mathrm{H},\,1}$	1.2×10^{21} cm$^{-2\dagger}$
$\log(\xi_{2,\,\mathrm{cgs}})$	$2.00\pm^{0.15}_{0.08}$
$N_{\mathrm{H},\,2}$	$(3.0 \pm 1.5) \times 10^{22}$ cm$^{-2\dagger}$
Collisional component	
kT	0.83 ± 0.02 keV
Power law	
Γ	1.66 ± 0.07
Total observed flux	
$\log(F_{0.5-2\,\mathrm{keV,\,cgs}})$	-12.157 ± 0.006

†unconstrained in the $10^{20\,-\,24}$ cm^{-2} range.

quality of the fit. Given the uncertainties on its origin, we do not discuss this feature in this paper, and do not include it in the soft X-ray model.

We then applied this soft X-ray baseline model to the 0.5–2 keV X-ray XIS spectra taken during the 2014–2015 observational campaign. The fits are satisfactory, just allowing for an overall normalization constant, C_{soft}, to vary. The best for values of C_{soft} are 0.99 ± 0.03, 0.96 ± 0.03, and 0.78 ± 0.03, for Obs.#709022010 to 709022040, respectively. Leaving the power-law spectral index free yields a significantly different value from that measured in 2005 only for Obs.#709022030: $\Gamma_{030} = 1.97\pm^{0.26}_{0.15}$, but the difference in the quality of the fit is marginal ($\Delta\chi^2 = 0.6$). This suggests only a small contribution of partial covering to the soft X-ray emission. Varying either the warm emitter ionization parameter or column density, or the power-law normalization at each epoch yields values always consistent with the common best fit.

The power-law component contributes over two orders of magnitude more than the other components to the flux above 4 keV. Consequently, in the model described in the following, we kept the soft X-ray baseline model parameters frozen to the values determined from the 0.5–2 keV *Suzaku*/XIS fit whenever *Suzaku* spectra are used; and allowed the normalization of the soft power law to vary within a dynamical range of ±20 per cent whenever *NuSTAR* data are analysed alone, or together with the EPIC-pn spectra. The EPIC-pn exposures discussed in this paper are too short to constrain the properties of the soft X-ray emission.

A detailed discussion of the variability of the soft X-ray spectrum of Markarian 3 is deferred to a future paper. More details on the soft X-ray spectroscopy can be found in: Sako et al. (2000), Bianchi et al. (2005b), Awaki et al. (2008), and Yaqoob et al. (2015).

4.2 `mytorus`-based models

We refrain in this paper from using purely empirical models to describe the broad-band X-ray spectra obtained during the 2014–2015 campaigns. The unprecedented combination of broad-band X-ray coverage and high sensitivity above 10 keV, coupled with the possibility of constraining the observables of the Fe Kα lines in those observations where *NuSTAR* and a CCD instrument were used quasi-simultaneously, allow us to constrain the parameter space of geometrically motivated models describing optically thick reprocessing of the primary continuum in this heavily obscured AGN. In this section, we make use of `mytorus` (Murphy & Yaqoob 2009), describing Compton-thick reprocessing in a toroidal geometry with a fixed half-opening angle $\theta_{\mathrm{op}} = 60^{\circ}$ and solar abundances. The assumed opening angle in `mytorus` is in good agreement with that expected if the torus in Markarian 3 follows the anticorrelation between X-ray luminosity and covering fraction observed in bright nearby Seyferts (Brightman et al. 2015). *NuSTAR* successfully constrained the properties of the AGN 'torus' in a number of heavily obscured AGN (Arevalo et al. 2014; Baloković et al. 2014; Gandhi et al. 2014; Puccetti et al. 2014; Bauer et al. 2015; Brightman et al. 2015; Rivers et al 2015; Marinucci et al. 2016).

Following Yaqoob et al. (2015), we fit the data using a 'decoupled scenario', described by the following equation:

$$M(E) = S(E) + A(N_{\mathrm{H,abs}}, E) \times (N_{\mathrm{po}} E^{\Gamma}) + C_{\mathrm{sc}} \times [R_{\mathrm{c}}(N_{\mathrm{H,sc}}) + R_{\mathrm{l}}(N_{\mathrm{H,sc}})] + \Sigma_i G_i(E_{\mathrm{l}}) \quad (1)$$

where $S(E)$ is the soft X-ray model described in Section 4.1; $\mathrm{A}(N_{\mathrm{H,\,abs}}, E$; model `mytorus_Ezero_v00.fits`) is an energy-dependent multiplicative factor describing the absorption of the primary continuum along the line of sight through a column density $N_{\mathrm{H,\,abs}}$, including the effect of Compton scattering. We parametrized the primary continuum with a simple power law with photon index Γ; R_{c} and R_{l} (models `mytorus_scatteredH500_v00.fits` and `mytl_V000010nEp000H500_v00.fits`) represent the scattered emission (in the continuum and in the line) due to the global column density $N_{\mathrm{H,\,sc}}$; C_{sc} takes into account differences between the transmitted primary continuum level and that illuminating the reflecting clouds; and G_i are Gaussian profiles describing a FeXXVI resonant absorption line, and a FeXXV emission line (see Section 4.5.2). In this scenario, the inclination angle of the Compton-scattered components is set to 0° (Yaqoob 2012). The inclination angle of the absorption table is a dummy parameter (fixed to 90° in the fit).

In the fitting procedure, we imposed that parameters not expected to vary over the time span covered by the monitoring campaign are tied together at all epochs ('global parameters', hereafter). They are: $C_{\mathrm{s},\,1}$ (the sub-script '1' indicates the first epoch in our monitoring campaign), $N_{\mathrm{H,\,sc}}$. The centroid energy of the absorption line was also frozen to 6.96 keV in the fit. The following astrophysical parameters were allowed to vary independently in each epoch: Γ, the power law normalization N_{po}, $N_{\mathrm{H,\,abs}}$ and the intensity of the absorption line I_{abs} ('epoch-dependent' parameters hereafter). Finally, we have made the assumption that the flux of the Compton scattering

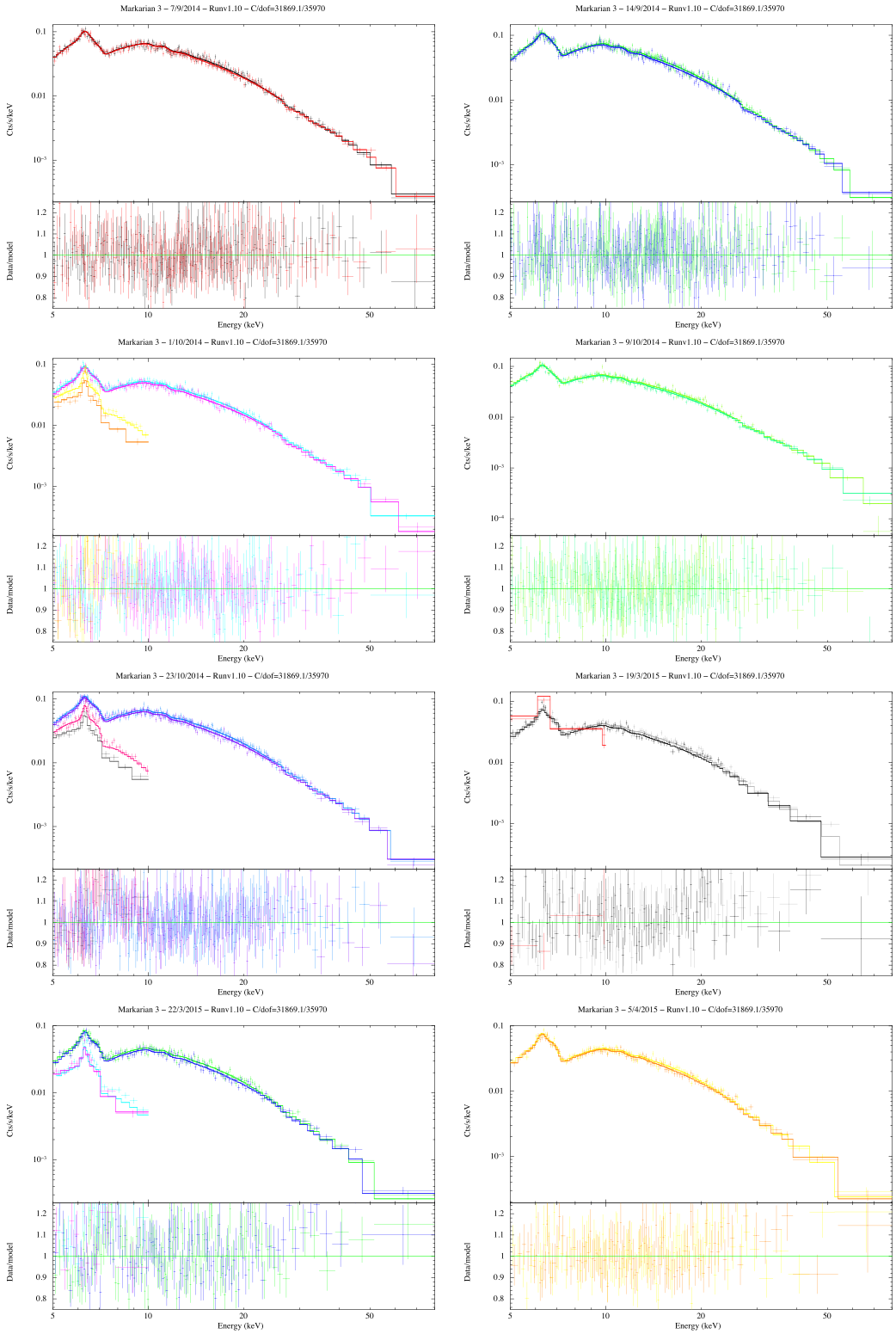

Figure 5. Spectra (upper panels) and residuals in units of data versus model ratio (lower panels) when the `mytorus` baseline model is fit to the epochs between 2014 September 7 and 2015 March 5. Where two spectra are shown, they correspond to the *NuSTAR*/FPM units; where three spectra are shown, the EPIC-pn spectrum is included; where four spectra are shown, the XIS spectra (BI and FI) are included.

and the intensity of the fluorescent line do not vary during our monitoring campaign, after verifying that this assumption is consistent with the data. We will refer to this model as the '`mytorus` baseline model' hereafter.

Fitting simultaneously the 26 spectra of the 2014–2015 Markarian 3 campaign with this model yields a good fit, with $C/\nu = 32\,004.0/35\,972$. The residuals are featureless (Fig. 5) in all observations. Possible enhancements do not significantly further

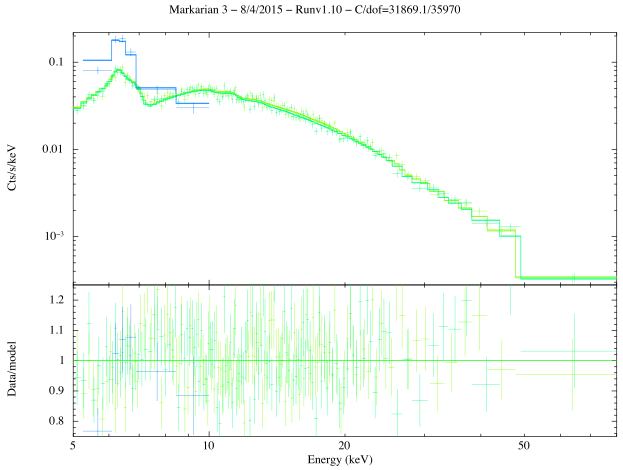

Figure 5 – *continued*

improve the quality of the fit: using `mytorus` components corresponding to lower values of the primary continuum high-energy cut-off (500 keV in the baseline model; this is consistent with the lower limit on the cut-off energy that we can set without data at the 99 per cent confidence level for two interesting parameters); allowing the centroid energy of the absorption line to be free (the best fit is always consistent with the rest-frame energy of Fe XXVI); or using a 'coupled scenario', i.e. a scenario where the column density and the inclination angles associated to all `mytorus` model components are tied together (the hypothesis of a fully homogeneous torus). At variance with the results of Yaqoob et al. (2015), the quality of the fit in 'coupled mode' is comparable to that obtained in 'decoupled mode' ($C/\nu = 31\,958.3/35\,973$), there is no systematic curvature in the residuals, and the best-fitting values of the intrinsic power-law photon index (1.77–1.93) are not particularly flat. However, it remains true that the best-fitting values of the column density vary among different epochs (in the range 2.64–3.26$\times$ 10^{24} cm^{-2}, with a typical statistical error $\simeq$0.03$\times$ 10^{24} cm^{-2}). Therefore, we rule out this scenario on astrophysical grounds, because it is difficult to explain how the global column density of the Compton scattering material could vary on time-scales as short as a few days.

Table 3 reports the epoch-dependent parameters in the `mytorus` baseline scenario. The line-of-sight column density varies between 7.5 and 9 $\times$ 10^{23} cm^{-2}, in agreement with the re-classification of Markarian 3 as 'Compton-thin' proposed by Yaqoob et al. (2015); the primary spectral index between 1.65 and 1.85, the normalization fluctuates about 30 per cent around its average. The `mytorus` baseline model requires a global column density $N_{\rm H,\,sc} = (1.16\pm^{0.08}_{0.11}) \times 10^{23}$ cm^{-2}. This is a factor of $\simeq$7 lower than the line-of-sight column density. A similar torus structure was inferred recently for ESO138-G0001 (De Cicco et al. 2015). Any deviation from a constant, isotropic illumination of the scattering clouds is, at most, modest: $C_{\rm sc,\,1} = (1.15 \pm 0.08)$. The intensity of the Fe XXVI absorption line is a factor of two larger in 2014 than in 2015. Its EW – calculated only against the primary transmitted continuum – is 10–20 eV in 2014, decreasing to $\lesssim$6 eV in 2015.

4.3 Ikeda-based models

Ikeda, Awaki & Terashima (2009; I09 hereafter) developed a Monte Carlo model to study the reflection-dominated spectra of heavily obscured AGN. I09 assume a spherical-toroidal geometry with a varying opening angle as opposed to the purely toroidal geometry of `mytorus`. The models therefore differ in their detailed predictions (Ricci et al. 2014). This sub-section discusses the application of the I09 models to the 2014–2015 Markarian 3 monitoring campaign, and compares its results with those obtained with `mytorus` in Section 4.2.

We run a series of fits in a configuration equivalent to the `mytorus` 'decoupled mode':

$$\begin{aligned} M(E) = {} & S(E) + A(N_{\rm H,abs},\,E) \times (N_{\rm po}E^{\Gamma}) \\ & + C_{\rm sc,1} \times [R_1(N_{\rm H,sc},\,\theta_{\rm incl},\,\theta_{\rm op}) + R_2(N_{\rm H,sc},\,\theta_{\rm incl},\,\theta_{\rm op}) \\ & + R_{\rm Fe}(N_{\rm H,sc},\,\theta_{\rm incl},\,\theta_{\rm op})] + \Sigma_i G_i(E_{\rm l}), \end{aligned} \quad (2)$$

where R_2 indicates the light reflected from the inner far side of the torus, and R_1 the remaining contribution to the continuum Compton-scattered emission. The Fe fluorescence component is embedded in $R_{\rm Fe}$. The free parameters in the Ikeda-based model are the same

Table 3. Best-fitting parameters for the epoch-dependent best-fitting parameters discussed in this paper.

Epoch	1	2	3	4	5	6	7	8	9
(YY/MN/DD)	14/09/07	14/9/14	14/10/01	14/10/09	14/10/23	15/03/19	15/03/23	15/04/05	15/04/08
`mytorus`									
Γ	$1.66\pm^{0.03}_{0.01}$	$1.69\pm^{0.02}_{0.01}$	$1.73\pm^{0.02}_{0.01}$	$1.72\pm^{0.03}_{0.01}$	$1.65\pm^{0.02}_{0.01}$	$1.81\pm^{0.07}_{0.07}$	$1.78\pm^{0.06}_{0.06}$	$1.85\pm^{0.04}_{0.03}$	$1.81\pm^{0.03}_{0.01}$
$N^a_{\rm po}$	$2.98\pm^{0.22}_{0.22}$	$3.67\pm^{0.24}_{0.04}$	$2.95\pm^{0.09}_{0.23}$	$3.58\pm^{0.25}_{0.21}$	$2.89\pm^{0.26}_{0.26}$	$3.37\pm^{0.21}_{0.56}$	$3.35\pm^{0.18}_{0.18}$	$4.46\pm^{0.31}_{0.41}$	$4.08\pm^{0.23}_{0.18}$
$N^b_{\rm H,abs}$	$0.77\pm^{0.01}_{0.01}$	$0.77\pm^{0.01}_{0.01}$	$0.81\pm^{0.01}_{0.01}$	$0.75\pm^{0.01}_{0.01}$	$0.74\pm^{0.01}_{0.01}$	$0.89\pm^{0.01}_{0.02}$	$0.87\pm^{0.01}_{0.01}$	$0.94\pm^{0.01}_{0.02}$	$0.90\pm^{0.01}_{0.02}$
Ikeda									
Γ	$1.76\pm^{0.02}_{0.01}$	$1.80\pm^{0.04}_{0.02}$	$1.81\pm^{0.01}_{0.03}$	$1.80\pm^{0.02}_{0.02}$	$1.73\pm^{0.02}_{0.02}$	$1.88\pm^{0.04}_{0.00}$	$1.85\pm^{0.01}_{0.01}$	$1.89\pm^{0.01}_{0.02}$	$1.87\pm^{0.01}_{0.02}$
$N^a_{\rm po}$	$2.79\pm^{0.10}_{0.08}$	$3.81\pm^{0.46}_{0.15}$	$2.53\pm^{0.13}_{0.21}$	$3.22\pm^{0.21}_{0.22}$	$2.70\pm^{0.13}_{0.14}$	$2.93\pm^{0.31}_{0.29}$	$2.74\pm^{0.15}_{0.15}$	$3.47\pm^{0.24}_{0.43}$	$3.44\pm^{0.18}_{0.18}$
$N^b_{\rm H,abs}$	$0.86\pm^{0.01}_{0.01}$	$0.92\pm^{0.01}_{0.01}$	$0.88\pm^{0.01}_{0.10}$	$0.86\pm^{0.01}_{0.01}$	$0.84\pm^{0.01}_{0.01}$	$1.01\pm^{0.02}_{0.03}$	$0.95\pm^{0.02}_{0.02}$	$1.08\pm^{0.02}_{0.02}$	$1.03\pm^{0.01}_{0.03}$
$I^c_{\rm abs}$	$-2.0\pm^{0.5}_{0.5}$	$-2.0\pm^{0.5}_{0.5}$	$-0.7\pm^{0.3}_{0.3}$	$-2.1\pm^{0.5}_{0.5}$	>-0.5	$-0.2\pm^{0.2}_{0.5}$	$-0.4\pm^{0.4}_{0.4}$	>-0.5	>-0.5
EW^d	$-20\pm^{5}_{6}$	$-15\pm^{4}_{4}$	$-8\pm^{4}_{5}$	$-18\pm^{5}_{6}$	>-6	$-1\pm^{1}_{4}$	$-4\pm^{4}_{5}$	>-6	>-6
$L_{\rm AGN}{}^e$	$4.21\pm^{0.15}_{0.09}$	$5.44\pm^{0.65}_{0.55}$	$3.52\pm^{0.13}_{0.25}$	$4.62\pm^{0.22}_{0.30}$	$4.25\pm^{0.20}_{0.21}$	$3.71\pm^{0.28}_{0.57}$	$3.62\pm^{0.14}_{0.47}$	$4.32\pm^{0.21}_{0.21}$	$4.41\pm^{0.15}_{0.36}$

[a] units of 10^{-2} photons cm^{-2} s^{-1} keV^{-1} at 1 keV
[b] units of 10^{24} cm^{-2}
[c] units of 10^{-5} photons cm^{-2} s^{-1}
[d] units of eV
[e] 2–10 keV luminosity of the transmitted component only, corrected for absorption, in units of 10^{43} erg s^{-1}

as in `mytorus`, with the addition of the torus half-opening angle ($\theta_{\rm op}$) and inclination angle ($\theta_{\rm incl}$). Moreover, the I09 line emission model does not include the Fe Kβ or the Ni emission lines. We thus included them in the model through phenomenological Gaussian profiles. The best-fitting ratio between Fe Kβ and the Fe Kα obtained with the models discussed in this section is $\simeq$7 per cent, with a statistical error of about 50 per cent. This value is lower, but still in broad agreement with the expectations from atomic physics (Molendi, Bianchi & Matt 2003). The constant ratio between the Ni Kα and the Fe Kα ($\simeq$20 per cent with a 50 per cent error bar) is instead larger than expected from the nickel-to-iron cosmic abundance (0.055–0.075). We refer to this model as the 'baseline Ikeda model' hereafter.

The fit to the 26 spectra of our monitoring campaign is marginally better than with `mytorus`-based models (C/ν = 31922/35969). In terms of best-fitting parameter values, the main differences with respect to the `mytorus` baseline can be summarized as follows:

(i) a 15 per cent higher line-of-sight column density (cf. Table 3), with a similar time variability pattern, but still consistent with a Compton-thin absorber;

(ii) a global column density larger by a factor of about 2 than the transmitted column density $N_{\rm H,\,sc} = (2.01\pm^{0.11}_{0.08}) \times 10^{24}$ cm^{-2}, with a scattering fraction $C_{\rm cs,\,1} = 1.00\pm^{0.05}_{0.08}$; and

(iii) a relatively wide torus ($\theta_{\rm op} = 66.0 \pm 0.4$) seen at an almost grazing angle ($\theta_{\rm incl} = 70 \pm 3^\circ$)

The best-fitting parameters of the Fe XXVI absorption line are very similar to those obtained with the `mytorus` baseline model. In Table 3, we show the line intensity $I_{\rm abs}$ and EW (calculated against the transmitted continuum only) obtained with the Ikeda baseline model.

4.4 `torus`-based models

We also fit the spectra of our monitoring campaign with the `torus` model (Brightman & Nandra 2011), a Monte Carlo simulation code based on the method of George & Fabian (1991) that assumes a biconical toroidal distribution similar to that employed in I09. This model can be used only in 'coupled mode', i.e. linking column density in transmission and in reflection. As already discussed in Section 4.2, `torus` cannot therefore be applied to our data in a fully self-consistent way. In spite of that, the column density best-fitting values are in the same range as those derived employing `mytorus`, and follow a very similar variability pattern as seen using the `mytorus` and the Ikeda models (Fig. 6). The torus properties derive with `torus` are in good agreement with that derived with I09. For instance, the best-fitting opening angle is $\theta_{\rm op} = 58 \pm 3^\circ$. This value is in good agreement with the correlation between X-ray luminosity and torus covering fraction measured in a sample of nearby heavily obscured AGN by *NuSTAR* (Brightman et al. 2015). The corresponding inclination angle ($\theta_{\rm incl} \geq 83^\circ$) is, however, significantly larger than with the I09 model, disfavouring a grazing view.

4.5 Comparison with previous observations

4.5.1 Suzaku 2005

Table 4 lists the best-fitting parameters obtained when the baseline Ikeda model is applied to the deep *Suzaku* observation of Markarian 3 in 2005 September (see I09 for a discussion on the application of the Ikeda model to the same observation). In performing the fit, we constrained the torus structural parameters ($N_{\rm H,\,sc}$, $\theta_{\rm op}$, $\theta_{\rm inc}$) within the confidence intervals determined from the 2014–2015 monitoring campaign, because they were determined with better precision than in previous studies. This assumes that the global structure of the pc-scale torus has not changed over the last decade. The fit is good (C/ν = 2952/2862). The continuum parameters are in broad agreement with those obtained during the 2014–2015 campaign. The line-of-sight column density is larger by a factor of $\simeq$70 per cent, changing the nominal source classification to a borderline Compton-thick object. The power-law normalization is lower by a factor of $\simeq$2, without this change being reflected in a proportional increase of the scattering fraction. No absorption line is detected in the energy range consistent with resonant transitions of He- or H-like iron.

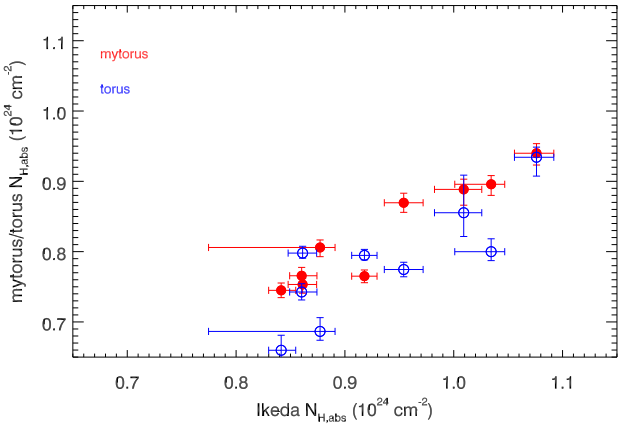

Figure 6. Comparison between the column density in transmission measured at the nine epochs of the 2014–2015 Markarian 3 monitoring campaign using I09 (*x*-axis), `mytorus` (*y*-axis, red filled points), and `torus` (*y*-axis, blue empty points).

Table 4. Best-fitting parameters when the `mytorus` baseline model is applied to the 2005 September *Suzaku* observation of Markarian 3.

Γ	$1.74\pm^{0.008}_{0.021}$
$N_{\rm po}$ (10^{-2} ph cm^{-2} s^{-1} keV^{-1})	$1.58\pm^{0.02}_{0.03}$
$N_{\rm H,\,abs}$ (10^{24} cm^{-2})	1.24 ± 0.03
$I_{\rm abs}$ (10^{-5} ph cm^{-2} s^{-1})	>-0.3
$C_{\rm sc}$	$1.24\pm^{0.16}_{0.05}$

4.5.2 Chandra*/HETG*

We downloaded from the TGCAT archive (Huenemoerder et al. 2011) the HETG spectra of Markarian 3 accumulated during the course of the *Chandra* mission, together with their associated background spectra and responses. These correspond to nine exposures[3] for a total net exposure time of about 778 600 s. They span a time range between 2000 March and 2011 April. The Medium-Energy Grating is insensitive above 5 keV. We therefore merged together the High-Energy Grating first order (positive and negative) spectra using the `addascaspectra` tool. The count rate in the 4–8 keV energy range is $(4.40 \pm 0.07) \times 10^{-3}$ s^{-1}, corresponding to 3402 net total counts. We determined that no variation in the continuum level below 6 keV, or in the intensity of the Fe Kα line is apparent in the spectra extracted from the individual *Chandra* observations.

[3] Observations numbers: 873, 12874, 12875, 13254, 13261, 13263, 13264, 13406, and 14331.

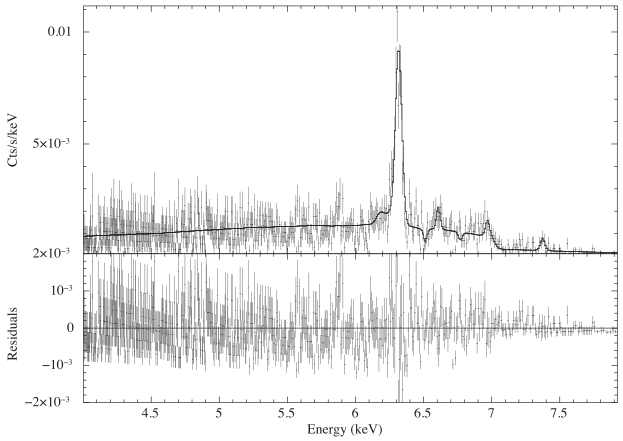

Figure 7. Markarian 3 *Chandra*/HETG time-averaged spectrum (crosses, upper panel) and residuals against the best-fitting model (lower panel). The solid line in the upper panel represents the Ikeda model-based best fit (details in the text).

Table 5. Best-fitting parameters when the model shown in Fig. 7 is applied to the *Chandra*/HETG time-averaged spectrum of Markarian 3.

Γ	>2.46
$N_{\rm po}$ (10^{-2} ph cm^{-2} s^{-1} keV^{-1})	8 ± 3
$N_{\rm H,\,abs}$ (10^{24} cm^{-2})	$1.29\pm^{0.18}_{0.03}$
$C_{\rm sc}$	$2.17\pm^{0.13}_{0.28}$
$I_{\rm emi}$ (10^{-5} ph cm^{-2} s^{-1})	0.4 ± 0.2
$I_{\rm abs,\,Fe\,XXV}$ (10^{-5} ph cm^{-2} s^{-1})	$-0.22\pm^{0.11}_{0.12}$
$I_{\rm abs,\,Fe\,XXVI}$ (10^{-5} ph cm^{-2} s^{-1})	>-0.16
σ (eV)	15 ± 4

The combined, time-averaged spectrum was fit in the 4–8 keV band using the Ikeda baseline continuum, and adding emission and absorption lines (modelled with simple Gaussian profiles) if statistically motivated at a confidence level larger than 90 per cent for one interesting parameter. We note that the I09 model includes the Compton shoulder. There is therefore no need of fitting this feature with ad hoc phenomenological profiles. In order not to overfit the data, we fixed the torus structural parameters ($N_{\rm H,\,sc}$, $\theta_{\rm op}$, $\theta_{\rm inc}$) to the values determined with the data of the 2014–2015 monitoring campaign. The final model requires one unresolved emission line, and two unresolved absorption lines. Their energies are consistent with Fe XXV recombination (6.7 keV, unconstrained), and Fe XXV ($6.60\pm^{0.06}_{0.08}$ keV) and Fe XXVI (6.96 keV, unconstrained) resonant absorption, respectively. The best fit is acceptable ($C/\nu = 672.4/584$), and does not show any systematic residual features (Fig. 7), especially in the iron band. The high resolution allows us also to constrain the width of the Fe Kα line. We did this by applying an energy-independent Gaussian convolution kernel to the best-fitting model. Its best-fitting width is $\sigma = 15 \pm 4$ eV, corresponding to 700 ± 200 km s^{-1} in velocity space. Table 5 shows the best-fitting parameters.

5 DISCUSSION

5.1 The origin of the hard X-ray variability in Markarian 3

In our previous paper on the recent X-ray history of Markarian 3, we (G12) proposed that the variability pattern of the 4–5 keV flux

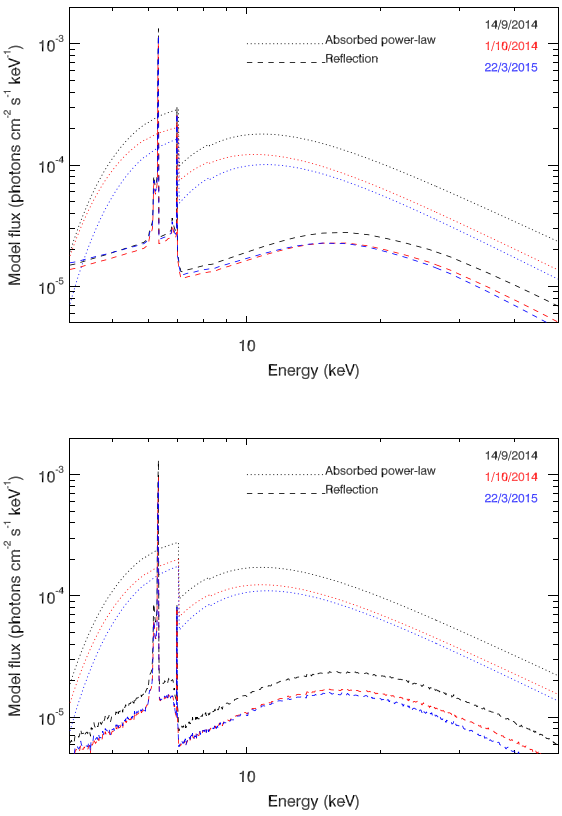

Figure 8. Best-fitting models in three epochs for the mytorus (top) and the Ikeda (bottom) best-fitting models in three epochs, in decreasing order of flux: 2014 September 14 (black), October 1 (red), and 2015 March 22 (blue). The dotted line represents the transmitted component, the dashed line the reflected component.

could be used to put constraints on the nature of the reprocessing matter. The results of the monitoring campaign reported in this paper rule out this claim, and contradict the idea that the spectral variability in this energy band can be used to constrain the properties of a Compton-thick reflector. Thanks to the accuracy in the spectral deconvolution allowed by the *NuSTAR* unprecedented combination of energy bandpass and spectroscopic quality above 10 keV, and to the usage of self-consistent physical models of the reprocessing, we achieve a more robust interpretation of the variability pattern. The continuum variability in the 4–50 keV band can be explained as due to the variation of the primary emission, (both in spectral index Γ and normalization $N_{\rm po}$, Fig. 8). As we will show in Sections 5.2.2 and 5.2.3, variability of the intervening absorber column density also contributes to the observed continuum variability. In these models, only the iron line traces the reflection component, while the 4–5 keV flux traces primarily that of the primary continuum in transmission with some dilution from the underlying reflection component. G12 had already remarked that the intensity of the Fe Kα lines does not track the 4–5 keV flux as would have been expected if they were both produced in the same reprocessing material. Fig. 8 provides us with a simple explanation of this observational fact.

Our results are in agreement with the systematic study of the X-ray variability in a sample of Seyfert 2 discussed by Hernández-García et al. (2015). These authors interpret the historical spectral variability in the *XMM–Newton* observations of Markarian 3 as primarily due to variations of the normalization of the primary power law. The limited bandpass of the *XMM–Newton* scientific payload prevented them from constraining the additional

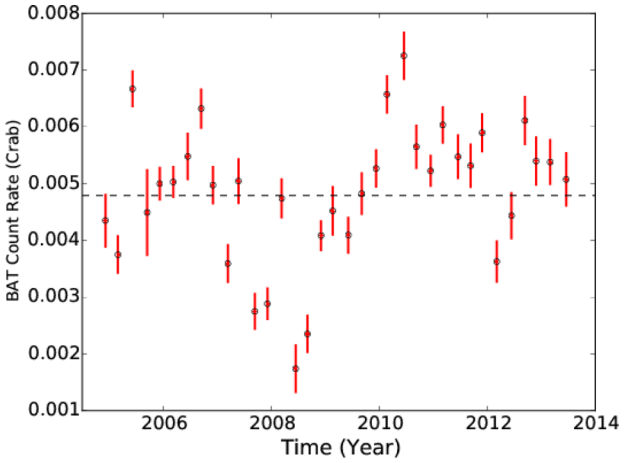

Figure 9. *Swift*/BAT light curve of Markarian 3 in the 14–195 energy band.

contribution due to variability of the intervening absorber column density. This can be fully unveiled in our campaign thanks to the extended coverage and hard X-ray unprecedented sensitivity of *NuSTAR*. In Hernández-García et al. (2015), Markarian 3 stands out as the only AGN classified as Compton-thick through indirect indicators showing variability in the 0.5–10 keV band. This lends additional support to the classification of Markarian 3 as a Compton-thin object (see also the discussion at the end of Section 5.2.1).

As the *Swift*/BAT light curve shows (Fig. 9), the AGN in Markarian 3 in one of the most variable in the X-ray band (G12). The overall dynamical range in the last decade has been a factor of about 8, with a doubling time on the order of 1 yr.

No significant intra-observation variability has been detected in the high-energy *NuSTAR* light curves of Markarian 3, at variance with, e.g. NGC 4945 (Puccetti et al. 2014). This is partly due to the lower statistics of the Markarian 3 data. The 30–79 keV Markarian 3 count rates during the 2014–2015 campaign were a factor of 2–10 lower than in NGC 4945. More fundamentally, Markarian 3 has been estimated to host a very massive black hole ($M_{\rm BH} \sim 4.5 \times 10^8$ M$_\odot$; Woo & Urry 2002). If its X-ray primary continuum follows the relation between power-spectrum break time-scale $T_{\rm B}$, black hole mass and luminosity established for unobscured AGN (McHardy et al. 2006):

$$\log(T_{\rm B}) = 2.1 \log(M_{\rm BH,6}) - 0.98 \log(L_{\rm bol,44}) - 2.28,$$

where $T_{\rm B}$ is in days, $M_{\rm BH,\,6}$ is in units of 10^6 M$_\odot$ and $L_{\rm b,\,44}$ is in units of 10^{44} erg s^{-1}, $T_{\rm B}$ is of the order of $\simeq$170 d. This indicates that little power is expected at frequencies comparable with the typical duration of *NuSTAR* observations with respect to the long-term behaviour.

We note in passing that a slight improvement in the quality of the fit in the `mytorus` scenario is obtained if $C_{\rm sc}$ is allowed to independently vary for each epoch ($\Delta C/\Delta\nu = 46.9/8$) with $C_{\rm sc}$ varying between 0.38 ± 0.08 in the highest flux state (2014 September 14) to 0.80 ± 0.11, $0.73^{0.18}_{0.15}$, and 0.77 ± 0.12 in the lowest flux states (2014 October 1 and 2015 March 19 and 23). However, it is hard to find a convincing astrophysical explanation for this finding. The mathematical interpretation of $C_{\rm sc}$ is complex. One should refrain from interpreting it as a simple covering fraction of the optically thick reprocessing matter (Murphy & Yaqoob 2009; Yaqoob 2012). It is rather a combination of the variability and anisotropy properties of the illuminating continuum, of the light crossing time delays between the illuminating source and the reprocessing matter, and of the detailed (and unknown) geometry of the reprocessing clouds. If the change in the $C_{\rm sc}$ values were solely due to a change in the property of the global reprocessing matter surrounding the central engine, one needs to invoke a mechanism to, for instance, more than double its column density or covering fraction between the second and the third observations in 2014, separated by 17 d. If due, for instance, to the onset of a disc wind at the virial escape velocity, $v_{\rm e} = (GM_{\rm BH}/r)^{0.5}$, and assuming that the wind clouds have to travel a distance at least comparable to the distance from the illuminating source to significantly contribute to the X-ray reflection, this wind should be launched at $r \sim 4 \times 10^{15}$ cm, or 70 gravitational radii, $r_{\rm g}$. Disc winds launched in the innermost regions of the accretion flows have been reported in some Seyfert Galaxies (Krongold et al. 2007), often with sub-relativistic outflow velocities (Tombesi et al. 2010). However, in this scenario, a correlation between the global wind covering factor and/or column density and the line-of-sight column density could be expected. Such a correlation is not seen in the data. While the complex nature of $C_{\rm s}$ may conceal it, accepting this interpretation would require ad hoc assumptions. We reject therefore this interpretation on astrophysical grounds.

5.1.1 On the correlation between accretion rate and spectral shape

A correlation between the accretion rate and the continuum spectral shape was recently discovered in intensity-resolved *NuSTAR* spectra of another nearby heavily obscured AGN, NGC 4945 (Puccetti et al. 2014). Similar correlations were found by comparing single-epoch spectra of large samples of type 1 AGN (Shemmer et al. 2008; Risaliti, Young & Elvis 2009; Brightman et al. 2013). Assuming a standard conversion factor of 30 between the 2 and 10 keV and the bolometric luminosity, $L_{\rm bol}$ (Elvis et al. 1994) the absorption-corrected X-ray AGN luminosity measured during the 2014–2015 campaign (Table 3) converts into an Eddington ratio $\lambda_{\rm Edd} \equiv L_{\rm bol}/L_{\rm Edd}$ between 1.9 per cent and 3.0 per cent. The dynamic range is too small for a correlation against the spectral index to be measurable, given the typical statistical errors in each epoch (Table 3). Conversely, the quality of time-resolved BAT spectra is insufficient to reliably measure a spectral index that could correlated with the larger flux dynamical range measured by *Swift*. The data points are broadly consistent with the locus in the Γ versus $\lambda_{\rm Edd}$ plane occupied by $z \lesssim 2$ AGN in the COSMOS and Extended *Chandra* Deep Field South surveys (Brightman et al. 2013).

5.2 X-ray constraints on the nature of the torus

5.2.1 X-ray time-averaged spectroscopy

Fitting the multi-epoch X-ray spectra of the Markarian 3 campaign with models of toroidal reprocessing yields constraints on the geometrical distribution of the optically thick matter. The Ikeda and the `torus` models require large opening angles, $\simeq$66° and $\simeq$58°, respectively. The baseline Ikeda model requires a grazing view along the rim of the torus ($\theta_{\rm incl} \simeq 70°$).

Taking into account the different geometries, the estimates of the torus opening angle are in the broad agreement with the opening angle assumed by `mytorus` (60°), making a comparison between the results obtained with the Ikeda and the `mytorus` models in the 'decoupled scenario' meaningful in principle. However, there is a serious tension between the Ikeda and `mytorus` models as far as the global column density out of the line of sight is concerned. The baseline Ikeda model requires a Compton-thick column of

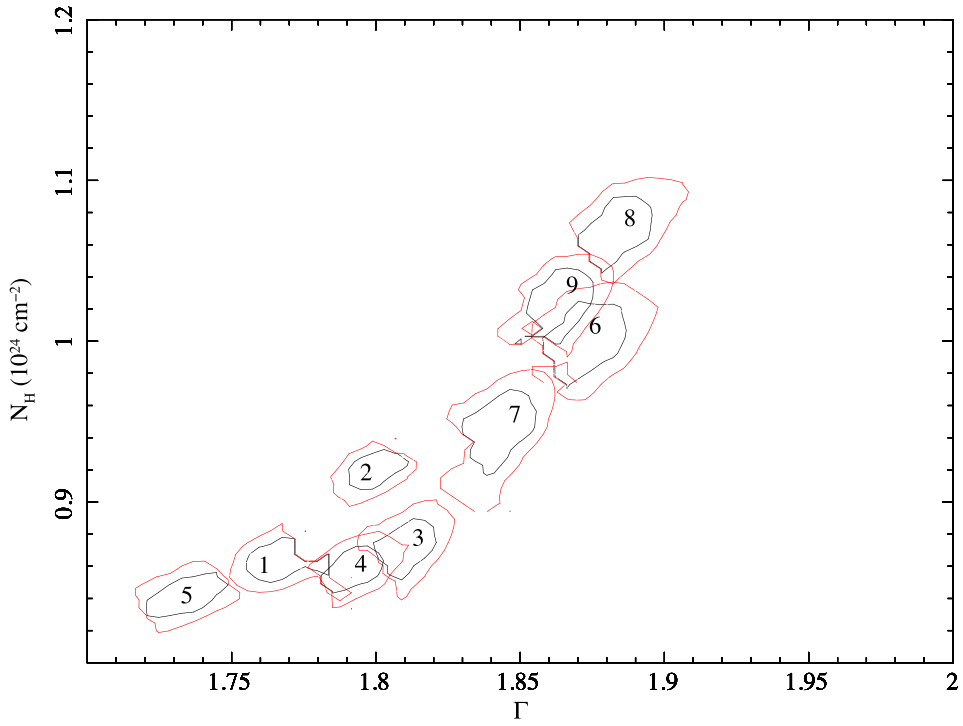

Figure 10. Iso-χ^2 contours for the photon index versus the line-of-sight column density obtained from the Ikeda best-fitting model applied to the spectra of the Markarian 3 2014–2015 monitoring campaign. The contours correspond to the 1σ and 90 per cent confidence levels for two interesting parameters. The integer number labels indicate the monitoring campaign epochs (cf. Table 1; 2014:1–5; 2015:6–9) and are placed at the locus corresponding to the best-fitting values.

$N_{\rm H,\,sc} \simeq 2.0 \times 10^{24}$ cm^{-2}, a factor of $\simeq$2–2.5 larger than the line-of-sight column density; the baseline `mytorus` model, instead, prefers a Compton-thin column ($N_{\rm H,\,sc} \simeq 1.2 \times 10^{23}$ cm^{-2}), a factor of 7–9 lower than the line-of-sight column density (Yaqoob et al. 2015). This tension is due to subtle differences in the curvature of the two models (cf. Fig. 8) over an energy range still dominated by the transmitted primary continuum in this source. The small difference in fit quality between the two scenarios does not allow us to prefer one solution on a purely statistical basis. If the torus in Markarian 3 is seen through a line of sight grazing the upper rim, however, one should expect the estimate of the global column density to exceed the column measured in transmission if the torus is thicker along the equatorial plane. On the basis of this geometrical argument, we consider the solution based on the Ikeda model more plausible on astrophysical grounds, and consider it as the reference solution in the forthcoming discussion.

Finally, we comment on the Markarian 3 classification with respect to the obscuration of its nucleus. Conventionally, the Compton-thin versus Compton-thick classification is based on the measured column density along the line of sight to the nucleus. We maintain this convention in this paper. As $N_{\rm H,\,abs}$ is always lower than 1.1×10^{24} cm^{-2} (Table 3), we conclude that Markarian 3 was in a Compton-thin state during the 2014–2015 monitoring campaign, even if the global column density estimated using the I09 model is higher than the Compton-thick threshold.

5.2.2 *Line-of-sight* $N_{\rm H}$ *variability: the 2014 occultation event*

Additional constraints on the nature of the torus clouds along the line of sight come from X-ray spectral variability. In Fig. 10, we show the iso-χ^2 contours for the photon index Γ versus the line-of-sight column density $N_{\rm H,\,abs}$ obtained from the Ikeda baseline model applied to the spectra of the Markarian 3 2014–2015 monitoring campaign. Using the two-dimensional contours allows us to estimate the dynamical range and time-scale of the line-of-sight column density variability, taking properly into account that this parameter is degenerate with the continuum shape in the spectral fitting procedure.[4] We obtain similar results if we plot the column density against the power-law normalization, or if we use the results obtained with the `mytorus` model. The column density shows two distinct variability patterns during the two sub-epochs of our monitoring campaign. We discuss these patterns separately in this, and in the following sub-section.

During the 2014 observations, the column density remains constant within the statistical uncertainty, with the exception of an increase by ($\Delta N_{\rm H} = (4.9 \pm 1.4) \times 10^{22}$ cm^{-2}) between the first (September 7) and second (September 14) observations, followed by a recovery to the original obscuration level on October 1. The most straightforward interpretation of this finding is an occultation event by a single additional cloud. Assuming that the total line-of-sight column density is due to the superposition of a system of identical (in $N_{\rm H}$) clouds, the total number of line-of-sight clouds can be constrained to 17 ± 5.

From the time-scale of this event $t_{\rm occ} \simeq 30$ d, we can estimate the distance of the occulting cloud from the X-ray source, R, under the assumption that its main velocity component is due to the orbital

[4] The Spearman ρ correlation coefficient (probability) is 0.97 (99.998 per cent), 0.90 (96 per cent), and 0.80 (80 per cent) for the full campaign, the 2014 and the 2015 observations, respectively.

velocity that can be well approximated by the Keplerian velocity at R:

$$v_k = \sqrt{\frac{GM_{\rm BH}}{R}} \quad (3)$$

where G is the gravitational constant. Assuming spherical symmetry and homogeneity, we can write an expression for R assuming that we can approximate the (unknown) size of the cloud $s \equiv v_k/t_{\rm occ}$ as $\simeq N_{\rm H}/n$, where n is the particle density (Lamer, Uttley & McHardy 2003; Risaliti et al. 2007; Svoboda et al. 2015):

$$R \simeq 1.6 \times 10^{14}\, M_{\rm Mkn3,BH}\, t^2_{\rm Mkn3,occ}\, \Delta N^{-2}_{\rm H,Mkn3}\, n_6^2 \ {\rm cm}, \quad (4)$$

where the 'Mkn3' sub-script indicates that we have expressed the corresponding quantity in units corresponding to the occultation event in Markarian 3. To close the system, we would need an estimate of the electron density of the cloud. We can make the additional assumption that the average ionization status of the occulting cloud is the same of the gas responsible for the bulk of the Fe Kα emission line. The centroid energy as measured in the *Chandra*/HETG spectrum is 6.396 ± 0.008 keV, while the energy of the photoabsorption edge in the same data is constrained to be 7.13 ± 0.03 keV. These measurements correspond to an Fe ionization state Fe$\leq$V (Kallman et al. 2004), or $\log(\xi) \lesssim -1.5$, where ξ is the ionization parameter $\equiv \frac{L}{nR^2}$ in cgs units, and L is the illuminating luminosity in the energy range 13.6 eV–13.6 keV ($\sim 1.1 \times 10^{44}$ erg s^{-1} in Markarian 3). Equation (4) would therefore imply a cloud at a distance $R \gtrsim 4 \times 10^{18}$ cm, with a density $n \lesssim 10^4$ cm^{-3}.

5.2.3 *Line-of-sight* $N_{\rm H}$ *variability in 2015*

During the 2015 observations, the line-of-sight column density variability pattern is more complex, and no clear individual occultation event can be identified. The largest $N_{\rm H}$ variation occurred between March 23 and April 5 ($\Delta N_{\rm H} = (1.3 \pm 0.3) \times 10^{23}$ cm^{-2}). A $\Delta N_{\rm H} = (5 \pm 3) \times 10^{22}$ cm^{-2} was measured between the two observations with the shortest separation (three days), still significant at the 90 per cent confidence level for two interesting parameters. We compared the 2015 $N_{\rm H}$ measurements with the expected Poissonian distribution due to an average number $N_{\rm c}$ of clouds with the same column density $N_{\rm H,c}$, and searched for the $N_{\rm c}$ maximizing the Kolmogornov–Smirnov probability that the observed measurements are extracted from that distribution. The maximum probability occurs for $N_{\rm H,c} = (3.2 \pm 0.4) \times 10^{22}$ cm^{-2}, or $N_{\rm c} = (32 \pm 4)$. While the assumptions behind this estimate are admittedly strong, as also confirmed by the shallow K-S probability ($\simeq$70 per cent), the resulting number of line-of-sight clouds is within a factor of 2 that derived from the single cloud occultation event in 2014.

5.3 Comparing the torus view in X-rays and IR

These results can be compared to the constraints on the torus structure derived from IR observations. The most complete study to date is based on Gemini/Michelle spectra at a resolution of 200 pc (Sales et al. 2014). Clumpy torus models (Nenkova et al. 2008) require an opening angle of 50°, seen at an inclination between 53° and 70° (best-fitting 66°). The inclination angles are in excellent agreement with those derived from X-ray spectroscopy. However, we stress that these results are obtained using a model with very different assumptions on the torus structure: clumpy in IR, homogeneous in X-ray models. Indeed, the mere detection of an occultation event during the 2014 campaign, and the line-of-sight absorbing column density variability observed during the 2015 campaign are clear indications of a torus clumpy structure in Markarian 3.

In the Nenkova et al. (2008) model, the torus is parametrized as a system of discrete clouds. Such a system is characterized by the average number of clouds along the torus equatorial plane; the visual optical depth of each cloud; the radial extension and profile of the cloud distributions, besides the inclination and the opening angles. The total column density of the IR clumpy torus in Markarian 3 was constrained to be $(5 \pm 3) \times 10^{23}$ cm^{-2} (Sales et al. 2014), i.e. a factor of 4 lower than the global column in X-rays in the baseline Ikeda model, and consistent with the `mytorus` baseline model. The average number of clouds in the equatorial plane ($6\pm^3_1$) corresponds to $4\pm^2_1$ along the estimated inclination angle to the torus (66°). Once again, this is a factor of about 3 lower than the number of line-of-sight clouds estimated through the study of the X-ray absorption variability pattern. Each of the IR-emitting clouds has an optical depth of 76 ± 12 mag, corresponding to $(1.7 \pm 0.3) \times 10^{23}$ cm^{-2}, i.e. a factor of about 4 larger.

Comparing the properties of the IR-emitting dust torus with that of the X-ray absorber/scatterer may indicate that the X-ray absorbing gas is largely within the dust sublimation radius. The mean dust sublimation radius for Silicate grains can be expressed as $r_{\rm sub} \sim L_{46}^{1/2} [T/1500\,{\rm K}]^{2.6} f(\phi)$ pc, where L_{46} is the AGN bolometric luminosity in units of 10^{46} erg s^{-1} and $f(\phi)$ is a geometrical factor equal to 1 for an isotropic source (Barvainis 1987). The absorption-corrected 2–10 keV AGN luminosity measured during the 2014–2015 campaign ranged between 3.5 and 5.4×10^{43} erg s^{-1} (the typical error on each measurement is between 10 per cent and 20 per cent). Assuming a bolometric correction of 30 (Elvis et al. 1994; Vasudevan & Fabian 2009), the dust sublimation radius is $\sim \times 10^{17}$ cm (0.4 pc).

However, such a conclusion relies on an admittedly crude understanding of the torus geometry. Other results presented in this paper point to a more complex and extended structure of the gaseous phase, either in the radial or in the vertical direction. If the occultation event in 2014 is due to a single cloud crossing our line of sight, it should be located at a distance of about 10 pc from the central engine (§ 5.2.2). IR spectroscopy suggests that torus extends to a radius of about 7 pc (Sales et al. 2014). Hence, such a cloud could belong to the torus outskirts. Another independent constraint on the location of the reprocessing gas comes from the width of the Fe Kα fluorescent line. Following Gandhi, Hönig & Kishimoto (2015), we estimate the emission radius of this line, $R_{\rm Fe}$, as

$$R_{\rm Fe} \equiv \frac{GM_{\rm BH}}{v^2},$$

where $v = \sqrt{3}/2 v_{\rm FWHM}$. Using the line width measured in the *Chandra*/HETG spectrum (§ 4.5.2), and applying the 2.3548 Gaussian conversion factor between standard deviation and full width at half-maximum, $R_{\rm Fe} \simeq 8 \pm 3$ pc (we assumed here a fiducial 25 per cent error on the black hole mass in this obscured AGN). This estimate is a factor of about 20 larger than the dust sublimation radius, $R_{\rm dust}$. This is in contrast to most of the AGN in the Gandhi et al. (2015) sample, where $R_{\rm Fe}$ is comparable or lower than $R_{\rm dust}$. We interpret this discrepancy in terms of line-of-sight orientation with respect to the torus axis. Most of the objects in the Gandhi et al. (2015) sample are Seyfert 1–1.9. They are not heavily obscured in X-rays, and are probably seen along small inclination angles. In Markarian 3, instead, the large inclination angle may prevent us from directly viewing the innermost regions of the torus in line emission. The bulk of the observed Fe line profile would therefore come from a more extended region, visible to us above the torus rim.

Such an interpretation could be validated by better Fe iron line data, allowing a more accurate decomposition of the line profile. This is impossible with the *Chandra*/HETG, but will be soon possible with the micro-calorimeter on board *ASTRO-H* (Mitsuda et al. 2012), thanks to its superb resolution and larger collecting area at the Fe line energies.

5.4 An ionized absorber in Markarian 3?

The baseline models during the 2014–2015 monitoring campaign require an absorption line around 7 keV (source frame) during most of the epochs. Its centroid energy is not very well constrained, but it is consistent with resonant absorption from H-like iron. This feature has never been reported in previous X-ray spectroscopic analysis of Markarian 3. Its presence is confirmed in the higher resolution HETG spectrum, where the single profile can be fit with complex structure composed of a recombination Fe XXV emission line, and two absorption lines whose centroid energies are consistent with resonant Fe XXV and Fe XXVI absorption. The intensity of the absorption lines in the *Chandra*/HETG spectrum is lower than observed in 2014, and consistent with that observed in 2015.

This feature could be the signature of a highly ionized absorption component along the line of sight to the AGN, possibly transient. A full characterization of the physical properties of this absorbing system is hampered by the quality of the data; insufficient, for instance, to assess if this absorption system is static or outflowing. From the theoretical standpoint, outflows are expected to arise in a disc atmosphere across or beyond the dust sublimation radius (Czerny & Hryniewicz 2011). Curve of growth analysis (Bianchi et al. 2005a; Risaliti et al. 2005) requires a column density $\lesssim 10^{22}$ cm^{-2} for the shallow absorption state measured in 2015, if the absorbing gas sees a Seyfert-like spectral energy distribution, and the turbulent velocity (unconstrained in our data) is lower than 500 km s^{-1}. This means that the absorber would be comparable to the 'warm absorbers' commonly observed in Seyfert Galaxies (McKernan, Yaqoob & Reynolds 2007; Laha et al. 2014), and probably launched at distances consistent with the innermost regions of the torus (Blustin et al. 2005). On the other hand, the column density estimate increases by at least one order of magnitude for the deeper features measured in 2014. Still, the constraints on the outflow velocity prevent the absorbing system in Markarian 3 from being identified as an ultra-fast outflow (Tombesi et al. 2010). We can compare it rather with the outflow detected in another (typically; Braito et al. 2014) heavily obscured AGN: NGC 1365 (Risaliti et al. 2005), where a system of four transitions were detected, corresponding to Kα and Kβ resonant absorption by He- and H-like iron. In Markarian 3, the EW is at least one order of magnitude lower than in NGC 1365, though.

The discovery of this highly ionized absorbing system is intriguing. It shows the not-often-detected simultaneous presence of cold optically thick obscuration and of an optically thin warm absorber in the same active galaxy. This provides indirect support for an origin of the ionized absorber as clouds evaporated at the outer surface of the torus (Kartje & Königl 1996; Blustin et al. 2005), and possibly accelerated by the radiation pressure due to the central AGN emission leaking through the patchy absorber. The existing anticorrelation between the line-of-sight column density and the warm absorber feature EW (cf. Table 3) lends support to this interpretation. Alternatively, the gas could be ionized along an absorption-free line of sight to the AGN, and fall back towards the equatorial plane in a failed jet or outflow (Ghisellini, Haardt & Matt 2004; Czerny & Hryniewicz 2011). However, one should bear in mind that Markarian 3 does host a radio jet (Pedlar, Unger & Booler 1984).

Future high-resolution measurements in the energy range where the Fe atomic transitions occur, such as those possible with the micro-calorimeter on board *ASTRO-H* (Mitsuda et al. 2012) will be crucial to properly characterize the physical properties of this absorbing system, and perform the required time-resolved diagnostics.

6 SUMMARY AND CONCLUSIONS

We report in this paper the results of an X-ray monitoring campaign of the heavily obscured Seyfert galaxy Markarian 3, carried out between the fall of 2014 and the spring of 2015 with *NuSTAR*, *Suzaku* and *XMM–Newton*. The campaign consisted of nine epochs, covering a wide range of time separations (and therefore of potential source variability time-scales) from about 3 d to 7 months. The campaign aimed at constraining the properties of the obscuring and reflecting material in this bright and highly variable AGN by comparing the X-ray spectra with geometrically motivated models of Compton scattering by optically thick matter in the AGN environs, as well as by analysing its extreme spectral variability on time-scales much shorter than studied so far (Iwasawa et al. 1994; G12).

The main results can be summarized as follows.

(i) The hard X-ray spectrum of Markarian 3 is variable on all the time-scales probed by our campaign, down to the shortest separation between consecutive observations (4 d; cf. Section 4).

(ii) We disprove the claim originally made by G12 (and already criticized by Yaqoob et al. 2015) that the X-ray spectral variability of the continuum below 10 keV can be used to constrain the properties of the optically thick re-processor in this object. This variability is due to a combination of a variation of the primary continuum (cf. Section 5.1) and of the intervening line-of-sight absorber column density (cf. Sections 5.2.2 and 5.2.3)

(iii) If arranged in a spherical-toroidal geometry as assumed by the Ikeda (I09) model, the Compton scattering torus has an opening angle $\simeq 66^\circ$, and is seen at a grazing angle through its upper rim (inclination angle $\simeq 70^\circ$). The global average column density is $\sim 2 \times 10^{24}$ cm^{-2}, keeping Markarian 3 in the rank of Compton-thick AGN, even if the line-of-sight column density measured during the monitoring campaign is in the Compton-thin range ($0.8–1.1 \times 10^{24}$ cm^{-2}; cf. Section 5.2.1).

(iv) We report the discovery of an increase of the line-of-sight column density during the 2014 observation, followed by a subsequent recovery to the pre-rise level. If due to an occultation event by a single cloud belonging to a system of clouds sharing the same column density, this event allows us to constrain their number (17 ± 5) and individual column density, [$(4.9 \pm 1.5) \times 10^{22}$ cm^{-2}] (cf. Section 5.2.2).

(v) While we cannot identify an occultation event during the 2015 campaign, the observed variability pattern of the line-of-sight column density is consistent within a factor of 2 with the geometrical and physical properties of the absorber as derived from the 2014 event (cf. Section 5.2.3).

(vi) The combination of the two previous pieces of evidence lends clear support to the clumpy nature of the torus in Markarian 3, as also indicated by the difference between the line of sight and global column density inferred by all models discussed in this paper.

(vii) The comparison between the derived properties of the obscuring gas and the properties of the IR-emitting dust (Sales et al.

2014) suggests that at least two-thirds of the X-ray obscuring gas volume might be located within the dust sublimation radius. However, the most dynamical clouds – such as those responsible for the occultation event in 2014 – are probably located on a larger scale, in the outskirts of the dusty torus (cf. Section 5.3). While the derived geometries of the IR- and X-ray material are similar, we stress that they were derived using different assumptions on the torus structure – clumpy in IR, homogeneous in X-ray models

(viii) We report the discovery of ionized absorber, characterized by variable resonant absorption lines due to He- and H-like iron. Markarian 3 is, to the best of our knowledge, the second object after NGC 1365 where an ionized absorber has been detected alongside heavy X-ray obscuration. This discovery lends support to the idea that moderate column density absorbers could be due to clouds evaporated at the outer surface of the torus, possibly accelerated by the radiation pressure due to the central AGN emission leaking through the patchy absorber (Czerny & Hryniewicz 2011, cf. Section 5.4) . The combination of iron absorption and emission features makes of Markarian 3 an ideal target to study the relation between torus reprocessing and the onset of ionized outflows with future high-resolution instruments such as the micro-calorimeter on board *ASTRO-H* (Mitsuda et al. 2012).

ACKNOWLEDGEMENTS

This work made use of data from the *NuSTAR* mission, a project led by the California Institute of Technology, managed by the Jet Propulsion Laboratory, and funded by the National Aeronautics and Space Administration. We thank the *NuSTAR* Operations, Software and Calibration teams for support with the execution and analysis of these observations. This research has made use of the *NuSTAR* Data Analysis Software (NUSTARDAS) jointly developed by the ASI Science Data Center (ASDC, Italy) and the California Institute of Technology (USA). JS acknowledges support from the grant LH14049 and the Project 14-20970P of the Grant Agency of the Czech Republic. FEB acknowledges support from CONICYT-Chile (Basal-CATA PFB-06/2007, FONDECYT Regular 1141218, 'EMBIGGEN' Anillo ACT1101), and the Ministry of Economy, Development, and Tourism's Millennium Science Initiative through grant IC120009, awarded to The Millennium Institute of Astrophysics, MAS. The authors are grateful to an anonymous referee, whose accurate and detailed report greatly improved the clarity of the paper.

REFERENCES

Antonucci R., 1993, ARA&A, 31, 473
Antonucci R. R. J., Miller J. S., 1985, ApJ, 297, 621
Arévalo P. et al., 2014, ApJ, 791, 81
Arnaud K. A., 1996, in Jacoby G., Barnes J., eds, ASP Conf. Ser. Vol. 101, Astronomical Data Analysis Software and Systems V. Astron. Soc. Pac., San Francisco, p. 101
Awaki H., Koyama K., Inoue H., Halpern J. O., 1991, PASJ, 43, 195
Awaki H. et al., 2008, PASJ, 60, S293
Baloković M. et al., 2014, ApJ, 794, 111
Barvainis R., 1987, ApJ, 320, 537
Bassani L., Dadina M., Maiolino R., Salvati M., Risaliti G., della Ceca R., Matt G., Zamorani G., 1999, ApJS, 121, 473
Bauer F. E. et al., 2015, ApJ, 812, 116
Bennett C. L. et al., 2003, ApJS, 148, 1
Bianchi S., Matt G., Nicastro F., Porquet D., Dubau J., 2005a, MNRAS, 357, 599
Bianchi S., Miniutti G., Fabian A. C., Iwasawa K., 2005b, MNRAS, 360, 380
Bianchi S., Maiolino R., Risaliti G., 2012, Adv. Astron., 2012, 17
Blustin A. J., Page M. J., Fürst S. V., Branduardi-Raymont G., Ashton C. E., 2005, A&A, 431, 111
Braito V., Reeves J. N., Gofforf J., Nardini E., Porquet D., Risaliti G., 2014, ApJ, 795, 87
Brightman M., Nandra K., 2011, MNRAS, 413, 1206
Brightman M. et al., 2013, MNRAS, 433, 2485
Brightman M. et al., 2015, ApJ, 805, 41
Burtscher L. et al., 2013, A&A, 558, 149
Cappi M. et al., 1999, A&A, 344, 857
Cash W., 1976, A&A, 52, 307
Chartas G., Kochanek C. S., Dai X., Pointdexer S., Garmire G., 2009, ApJ, 693, 174
Collins N. R., Kraemer S. B., Crenshaw D. M., Bruhweiler F. C., Meléndez M., 2009, ApJ, 694, 765
Czerny B., Hryniewicz H., 2011, A&A, 525, L8
De Cicco M., Marinucci A., Bianchi S., Piconcelli E., Violino G., Vignali C., Nicastro F., 2015, MNRAS, 453, 2155
Elvis M. et al., 1994, ApJS, 95, 1
Foster A. R., Ji L., Smith R. K., Brickhouse N. S., 2012, ApJ, 756, 128
Gabriel C., Denby M., Fyfe D. J., Hoar J., Ibarra A., 2003, in Ochsenbein F., Allen M., Egret D., eds, ASP Conf. Ser. Vol. 314, Astronomical Data Analysis Software and Systems XIII. Astron. Soc. Pac., San Francisco, p. 759
Gandhi P. et al., 2014, ApJ, 792, 117
Gandhi P., Hönig S. F., Kishimoto M., 2015, ApJ, 812, 113
George I. M., Fabian A. C., 1991, MNRAS, 249, 352
Ghisellini G., Haardt F., Matt G., 2004, A&A, 413, 535
Guainazzi M., La Parola V., Miniutti G., Segreto A., Longinotti A., 2012, A&A, 547, 31 (G12)
Harrison F. A. et al., 2013, ApJ, 770, 103
Hernández-García L., Masegosa J., González-Martin O., Márquez I., 2015, A&A, 579, 90
Huenemoerder D. P. et al., 2011, AJ, 141, 129
Ikeda S., Awaki H., Terashima Y., 2009, ApJ, 692, 608 (I09)
Ishida M. et al., 2011, PASJ, 63, 657
Iwasawa K., Yaqoob T., Awaki H., Ogasaka Y., 1994, PASJ, 46, L167
Jaffe W. et al., 2004, Nature, 429, 47
Jun H. D., Stern D., Graham M. J., Djorgovski S. G., Mainzer A., Cutri R. M., Drake A. J., Mahabal A. A., 2015, ApJ, 814, 12
Kalberla P. M. W., Burton W. M., Hartmann D., Arnal M., Bajaja E., Morras R., Pöppel W. G. L., 2005, A&A, 440. 775
Kallman T. R., Palmieri P., Bautista M. A., Mendoza C., Krolik J. H., 2014, ApJS, 155, 675
Kallman T. R., Evans D. A., Marshall H., Canizares C., Longinotti A., Nowak M., Schulz N., 2014, ApJ, 780. 121
Kartje J. F., Königl A., 1996, Vistas Astron., 40, 133
Khachikian E. Y., Weedman E. W., 1974, ApJ, 192, 581
Kishimoto M., Hönig S. F., Beckert T., Weigelt G., 2007, A&A, 476, 713
Koshida S. et al., 2014, ApJ, 788, 159
Koyama K. et al., 2007, PASJ, 59, 23
Krongold Y., Nicastro F., Elvis M., Brickhouse N. S., Binette L., Mathur S., Jiménez-Bailón E., 2007, ApJ, 659, 1022
Laha S., Guainazzi M., Dewangan G., Chakravorty S., Kembhavi A., 2014, MNRAS, 441, 2613
Lamer G., Uttley P., McHardy I. M., 2003, MNRAS, 342, L41
Lampton M., Margon B., Bowyer S., 1976, ApJ, 207, 894
McHardy I., Koerding E., Knigge C., Uttley P., Fender R. P., 2006, Nature, 444, 730
McKernan B., Yaqoob T., Reynolds C. S., 2007, MNRAS, 379, 1359
Madsen K. et al., 2015, ApJS, 220, 8
Marinucci A. et al., 2016, MNRAS, 456, L94
Markowitz A. G., Krumpe M., Nikutta R., 2014, MNRAS, 439, 1403
Mitsuda K. et al. J. Low Temp. Phys., 167, 795
Molendi S., Bianchi S., Matt G., 2003, MNRAS, 343, L1
Morgan C. W. et al., 2012, ApJ, 756, 52
Murphy K., Yaqoob T., 2009, MNRAS, 397, 1549

Nenkova M., Sirocky M. M., Nikutta R., Ivezić Z., Elitzur M., 2008, ApJ, 685, 160
Netzer H., 2015, ARAA, 53, 1
Netzer H., Laor A., 1993, ApJ, 404, 51
Pedlar A., Unger S. W., Booler R. V., 1984, MNRAS, 207, 193
Pounds K. A., Page K. L., 2005, MNRAS, 360, 1123
Pozo-Nuñez F. et al., 2014, A&A, 568, 36
Puccetti S. et al., 2014, ApJ, 793, 26
Ricci C., Ueda Y., Paltani S., Ichikawa K., Gandhi P., Awaki H., 2014, MNRAS, 441, 3622
Risaliti G., Bianchi S., Matt G., Baldi A., Elvis M., Fabbiano G., Zezas A., 2005, ApJ, 630, L129
Risaliti G., Elvis M., Fabbiano G., Baldi A., Zezas A., Salvati M., 2007, ApJ, 659, L111
Risaliti G., Young M., Elvis M., 2009, ApJ, 700, 6
Rivers E. et al., 2015, ApJ, 805, 55
Sako M., Kahn S. M., Paerels F., Liedahl D. A., 2000, ApJ, 543, L115
Sales D. A., Ruschel-Dutra D., Pastrorizas M. G., Riffel R., Winge C., 2014, MNRAS, 441, 630
Shemmer O., Brandt W. N., Netzer H., Maiolino R., Kaspi S., 2008, ApJ, 682, 81
Strüder L. et al., 2001, A&A, 365, L18
Suganuma M. et al., 2006, ApJ. 639, 46
Svoboda J., Beuchert T., Guainazzi M., Longinotti A. L., Piconcelli E., Wilms J., 2015, A&A, 578, 96
Tombesi F., Cappi M., Reeves J.N., Palumbo G. C. C., Yaqoob T., Braito V., Dadina M., 2010, A&A. 521, 57
Torricelli-Ciamponi G., Pietrini P., Risaliti G., Salvati M., 2014, MNRAS, 442, 2116
Vasudevan R. V., Fabian A. C., 2009, MNRAS, 392, 1124
Woo J.-H., Urry M. C., 2002, ApJ, 579, 530
Yaqoob T., 2012, MNRAS, 423, 3360
Yaqoob T., Tatum M. M., Scholtes A., Gottlieb A., Turner T. J., 2015, MNRAS, 454, 973

[1]*Institute of Space and Astronatical Science (JAXA), 3-1-1 Yoshinodai, Sagamihara, Kanagawa, 252-5252, Japan*
[2]*European Space Astronomy Center of ESA, PO Box 78, Villanueva de la Cañada, E-28691 Madrid, Spain*
[3]*INAF – Osservatorio di Arcetri, Largo E. Fermi 5, I-50125 Firenze, Italy*
[4]*Dipartimento di Fisica e Astronomia, Università di Firenze, Via G. Sansone 1, I-50019, Sesto Fiorentino (Firenze), Italy*
[5]*Department of Physics, Ehime University, Matsuyama 790-8577, Japan*
[6]*Instituto de Física y Astronomía, Facultad de Ciencias, Universidad de Valparaíso, Gran Bretana N 1111, Playa Ancha, Valparaíso, Chile*
[7]*Instituto de Astrofísica, Facultad de Física, Pontificia Universidad Católica de Chile, Casilla 306, Santiago 22, Chile*
[8]*Millennium Institute of Astrophysics (MAS), Nuncio Monseñor Sótero Sanz 100, Providencia, Santiago, Chile*
[9]*Space Science Institute, 4750 Walnut Street, Suite 205, Boulder, CO 80301, USA*
[10]*Dipartimento di Matematica e Fisica, Università degli Studi Roma Tre, via della Vasca Navale 84, I-00146 Roma, Italy*
[11]*Space Sciences Laboratory, University of California, Berkeley, CA 94720, USA*
[12]*Department of Astronomy and Astrophysics, The Pennsylvania State University, 525 Davey Lab, University Park, PA 16802, USA*
[13]*Institute for Gravitation and the Cosmos, The Pennsylvanya State University, University Park, PA 16802, USA*
[14]*Department of Physics, 104 Davey Lab, The Pennsylvania State University, University Park, PA 16802, USA*
[15]*Cahill Center for Astrophysics, California Institute of Technology, 1216 East California Boulevard, Pasadena, CA 91125, USA*
[16]*DTU Space – National Space Institute, Technical University of Denmark, Elektrovej 327, DK-2800 Lyngby, Denmark*
[17]*Lawrence Livermore National Laboratory, Livermore, CA 94550, USA*
[18]*Columbia Astrophysics Laboratory, Columbia University, New York, NY 10027, USA*
[19]*Department of Physics, Institute for Astronomy, ETH Zurich, Wolfgang-Pauli-Strasse 27, CH-8093 Zurich, Switzerland*
[20]*Catedrática CONACYT – Instituto Nacional de Astrofísica, Óptica y Electrónica, Luis E. Erro 1, Tonantzintla, Puebla, C.P. 72840, México*
[21]*NASA Goddard Space Flight Center, Greenbelt, MD 20771, USA*
[22]*Department of Astronomy, University of Maryland, College Park, MD 20742, USA*
[23]*NASA Jet Propulsion Laboratory, 4800 Oak Grove Dr, Pasadena, CA 91109, USA*
[24]*Astronomical Institute, Academy of Sciences, Boční II 1401, CZ-14100 Prague, Czech Republic*

This paper has been typeset from a TEX/LATEX file prepared by the author.